Colloquium: Geometry and optimal packing of twisted columns and filaments

Gregory M. Grason

Department of Polymer Science and Engineering, University of Massachusetts, Amherst, Massachusetts 01003, USA

(published 14 May 2015)

This Colloquium presents recent progress in understanding constraints and consequences of close-packing geometry of filamentous or columnar materials possessing nontrivial textures, focusing, in particular, on the common motifs of twisted and toroidal structures. The mathematical framework is presented that relates spacing between linelike, filamentous elements to their backbone orientations, highlighting the explicit connection between the interfilament *metric* properties and the geometry of non-Euclidean surfaces. The consequences of the hidden connection between packing in twisted filament bundles and packing on positively curved surfaces, like the Thomson problem, are demonstrated for the defect-riddled ground states of physical models of twisted filament bundles. The connection between the "ideal" geometry of *fibrations* of curved three-dimensional space, including the Hopf fibration, and the non-Euclidean constraints of filament packing in twisted and toroidal bundles is presented, with a focus on the broader dependence of metric geometry on the simultaneous twisting and folding of multifilament bundles.

DOI: 10.1103/RevModPhys.87.401 PACS numbers: 61.72.Lk, 61.30.Mp, 87.16.Ka, 81.05.Lg

CONTENTS

I. INTRODUCTION

Geometrical models of matter have been a cornerstone of physical theories of materials for centuries. Like Kepler's hypothesis that the emergent symmetries of crystals derive from optimal packings of hard-spherical "atoms" (Hales, 2000), such models connect the collective physical properties of microscopic particles and molecules to principles of packing of elementary geometrical objects. From the statistical mechanics of n-body clusters in hard-sphere gases and fluids (McQuarrie, 2000) to properties of granular and amorphous behavior deriving from the so-called random close-packed state (Bernal and Mason, 1960; O'Hern *et al.*, 2003), connections between the geometry of sphere packing and many-body behavior of compact, isotropic particles pervades condensed matter. By comparison, the generic principles and emergent behavior of a parallel class of models, what we call *filamentous matter*, remains largely unknown. Filamentous matter refers to assemblies of multiple one-dimensional or linelike elements, a geometrical motif that appears in diverse materials and formed at a range of dimensions spanning nearly 7 orders of magnitude in size (Pan, 2014). Ropes, cables, and textiles are familiar examples from macroscopic materials (Hearle, Grosberg, and Backer, 1969; Costello, 1997), and physical considerations of the role their structure plays in emergent mechanical properties like tensile strength date back to at least as early as Galileo's work on the strength of materials (Galileo, 1914). With the advent of modern microscopy came the discovery that ropelike and fabriclike assemblies of macromolecular filaments constitute a crucial and broad class of structure elements of biological matter, from the cytoskeleton to extracellular tissue.

This Colloquium reviews recent theoretical advances in understanding the structure formation of cohesive filament assemblies, with the particular focus on how the geometrical interplay between orientation and interfilament spacing shape the nontrivial structural and thermodynamic properties of assemblies. Of primary interest are an important class of "self-twisting" assemblies of filaments or columns, whose complex textures are driven by molecular chirality. The interplay between chirality and long-range ordering is a subject of long-standing interest in condensed matter, and in liquid crystals, in particular (de Gennes and Prost, 1993). Intermolecular forces between chiral molecules favor textures with nontrivial, and twisted, gradients in orientation (Goodby, 1991; Harris, Kamien, and Lubensky, 1999), the simplest example of which is cholesteric order. Crucially, the patterns of orientation driven by chirality are not always compatible with other types of ordering exhibited by a given system, as in chiral smectics (de Gennes, 1972; Renn and Lubensky, 1988; Goodby, 2012), or even with the geometrical constraints of space itself (Sadoc and Mosseri, 2008) as occurs for the double-twist textures of the liquid crystal blue phases (Sethna, Wright, and Mermin, 1983; Wright and Mermin, 1989).

The interplay between chiral patterns of orientation and long-range, 2D ordering of columns or filaments combines these two aspects of frustration. For example, theories of chiral columnar liquid crystals show that uniform twist of column backbones and lattice directions, both of which are favored by chirality, are incompatible with bulk columnar ordering (Kamien and Nelson, 1995, 1996). Because chiral textures are *globally incompatible* with long-range 2D positional order, in sufficiently chiral bulk systems, twisted textures can be accommodated only through the introduction of complex networks of tilt-grain boundaries. The focus of this Colloquium is a related, but distinct, frustration between orientation and 2D positional order that occurs in finite domains with nontrivial textures, in particular, within the twisted structures shown in Fig. 1. Simply put, as one among a broader class of such textures, twist makes it geometrically impossible to evenly space filaments or columns, even locally, throughout the domain cross section (Kléman, 1980; Starostin, 2006).

In filamentous matter, frustration follows from an intrinsic geometric coupling between the orientation and spacing of linelike materials, a relationship which therefore has implications for the structure and thermodynamics of a broad range of self-organized systems. These include columnar forming liquid crystals, such as lyotropic chromonics [Fig. 1(i)], which exhibit complex and twisted textures upon confinement (Tortora and Lavrentovich, 2011; Jeong *et al.*, 2014). When columnar droplets form in a dense chromonic suspension, the chainlike nature of columns promotes tangential anchoring within droplets, which is known to stabilize toroidal or spontaneously twisted topologies in even achiral chainlike systems (Svenšek, Veble, and Podgornik, 2010; Shin and Grason, 2011). Further examples include twisted and hexagonally packed wormlike assemblies of chiral (or achiral) surfactant micelles, which have become an important and widely studied route to chiral mesoporous silica structures [Fig. 1(e)] and provide perhaps the most robust platforms for multiscale imaging of twisted columnar packing (Che *et al.*, 2004; Yang *et al.*, 2006).

Beyond columnar systems *per se*, cohesive assemblies of two-dimensionally packed filaments constitute a basic materials architecture in both biological and synthetic systems, relevant to a broader materials context. In living organisms, assemblies of filamentous proteins represent a primary structural motif, from bundles of cytoskeletal filaments to fibers of extracellular proteins (Alberts *et al.*, 2002). Biological filaments are universally helical in structure, owing to the underlying chirality of their constituent macromolecules, proteins, and polysaccharides (Bouligand, 2008; Hamley, 2010). Hence, ropelike assembles of protein filaments often exhibit a tendency to twist in a handed fashion (Grason and Bruinsma, 2007; Grason, 2009; Yang, Meyer, and Hagan, 2010; Heussinger and Grason, 2011). The chiral textures of filamentous protein bundles and fibers have been the subject of extensive study in numerous systems, from fibrin (Weisel, Nagawami, and Makowski, 1987; Weisel, 2004) and fibrillar collagen (Cooper, 1969; Bouligand *et al.*, 1985; Ottani *et al.*, 2002; Wess, 2008) to extracellular chitan, cellulose fibers (Neville, 1993) and sickle hemoglobin macrofibers (Makowski and Magdoff-Fairchild, 1986). Beyond structural biofilaments, dsDNA is known to exhibit columnar order at very high concentrations (Livolant *et al.*, 1989), as well as chirally ordered mesophases (Livolant and Leforestier, 1996). Furthermore, upon condensation (Hud, Downing, and Balhorn, 1995; Hud and Downing, 2001) or under confinement (Knobler and Gelbart, 2009; Leforestier and Livolant, 2009, 2010), dense states of DNA exhibit a range of complex topologies, from

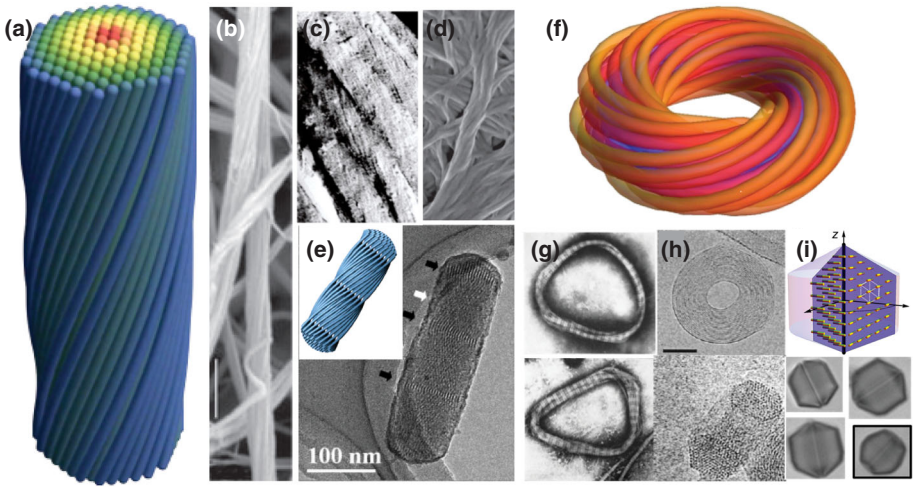

FIG. 1 (color online). (a)–(e) Twisted bundles (a)of filaments or columns in biological and synthetic materials [electron microscope (EM) images in (b)–(e))]: (b) fibrin bundles (diameter ∼100 nm) (Weisel, 2004); (c) twisted collagen fibrils derived from tendon (diameter ∼100 nm) (Ottani *et al.*, 2002); (d) twisted fibers of chiral organogel assemblies (diameter ∼100 nm) (Foster *et al.*, 2010); and (e) mesoporous silica templated by twisted columnar assemblies of wormlike surfactant micelles, with schematic in the inset (diameter ∼100 nm) (Yang *et al.*, 2006). (f)–(i) Toroidal bundles [schematic of twisted toroidal bundle in (f)] of filaments or columns from biological and synthetic materials: (g) EM images of twisted toroidal fibers of collagen (Cooper, 1969); (h) EM images of toroidal condensates of dsDNA (Hud and Downing, 2001); and (i) schematic and optical microscopy of faceted columnar droplets of chromonic liquid crystals (Jeong *et al.*, 2014).

twisted to folded tori. Outside of the strictly biological contexts, synthetic materials, from peptide-based biomaterial mimics (Kouwer *et al.*, 2013) to organogelators and supramolecular polymers (Douglas, 2009; Lee *et al.*, 2009), offer numerous further examples of the self-twisted and densely packed filament and fibers.

The preponderance of distinct materials exhibiting twisted and densely packed filaments or columns motivates a series of basic questions regarding the common, underlying geometric principles that constrain their structure. How does the nontrivial geometry (e.g., twist, bend, etc.) of a columnar assembly influence the structure and energetics of lateral order? What are the optimal packings of filaments for a given nontrivial assembly geometry, and what factors (geometric, mechanical, molecular) determine these states? In this Colloquium, recent theoretical progress in understanding optimal order in twisted columnar and filamentous materials as well as the nonlinear interplay between orientation and spacing in columnar systems is discussed, more generally. In particular, this Colloquium focuses on understanding how certain patterns of filament orientation are incompatible with homogeneous interfilament spacing, leading to a frustration of long-range 2D order that is quite analogous to frustration of positional order on intrinsically curved surfaces, such as spheres. The principal goal is to review theoretical frameworks for analyzing constraints of interfilament spacing deriving from nonuniform textures of two specific types: twisted, cylindrical bundles [Fig. 1(a)] and twisted toroidal bundles [Fig. 1(f)]. An important focus is models that quantify the thermodynamics costs of nonuniform filament spacing in these *incompatible textures*, as well as the nature of the inhomogeneous filament packings that constitute the ground states of these frustrated textures.

This Colloquium is organized as follows. Section II begins with an introduction to a notion of interfilament spacing and metric properties of multifilament structures in the continuum limit of infinitesimal spacing. Section III focuses on the unique metric geometry of twisted bundles, relating the constraints of interfilament packing to those constraining packing on a curved 2D surface, and reviews predictions for the number, type, and distribution of defects in the lateral packing of ground-state bundles. Section IV reviews theoretical approaches to the structure of twisted toroidal bundles based on ideal properties of filament packings in S^3, the three-dimensional hypersphere. We conclude with a brief discussion of outstanding challenges for understanding optimal packing of filaments and columns beyond the twisted textures considered in this Colloquium.

This Colloquium makes extensive use of concepts and methods of classical differential geometry of curved 2D surfaces, principally, the notion of surface metrics and their relation to the intrinsic, or Gaussian curvature. Though this Colloquium relies primarily on graphical descriptions where possible, a reader unaccustomed to these elementary concepts of different geometry may find it useful to refer to an introductory text (Millman and Parker, 1977) or "primer" (Kamien, 2002) on the subject.

II. CHARTING THE METRIC PROPERTIES OF INTERFILAMENT PACKING, A CONTINUUM PERSPECTIVE

In this section we illustrate constraints of interfilament packing deriving from arbitrary, nonuniform textures of filament orientation, and, in particular, the connection of these constraints to the metric geometry of 2D curved surfaces (Millman and Parker, 1977). Like membranes or sheets, filaments and columns are extended objects. Hence, not unlike multilayered or smectic materials, notions of interfilament distance are intimately connected to filament orientation. Even when interfilament forces are short ranged, the nature of interfilament contact is fundamentally nonlocal. This is because the relevant "distance" between a given point, say on one filament, and another filament, say its neighbor, typically refers to the distance of closest approach, a quantity that depends nonlinearly on shape and orientation.

In collections of filaments, as in condensed phases of multifilament systems or columnar assemblies, the texture of filament orientations is intrinsically linked to metric (i.e., spacing) properties of interfilament packing, quite analogous to the way the geometry, or curvature, of a 2D surface constrains the spacing between material points upon it. To understand this connection, we consider an ensemble of filaments that are, on average, oriented normal to the x-y plane (see Fig. 2). Here we focus on the continuum limit, where density is sufficiently high so that filaments are locally parallel and subject to only gradual variation of orientation throughout the packing. Specifically, we assume that variations of shape and orientation between neighboring filaments are negligible on the scale of interfilament spacing, set by the diameter d. The spacing between two neighboring filaments α and β whose center lines are described by curves $\mathbf{R}_\alpha(s_\alpha)$ and $\mathbf{R}_\beta(s_\beta)$, and which intersect the plane at height z at s_α^0 and s_β^0, respectively (see Fig. 2). The distance of closest approach from α to β is determined by optimizing the separation between these curves over positions on the second filament, resulting in an interfilament vector that is, by definition, perpendicular to $\mathbf{R}_\beta$ at the point of contact. To determine the point of contact

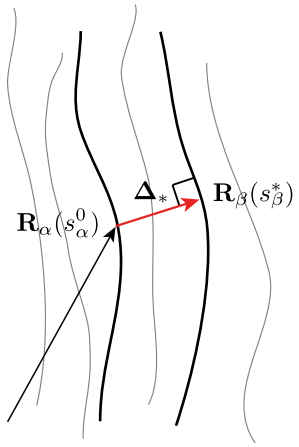

FIG. 2 (color online). Local distance of closest approach $\mathbf{\Delta}_*$ between filament α at s_α^0 to filament β, where s_β^* is the closest point to $\mathbf{R}_\alpha^0$.

from $\mathbf{R}^0_\alpha \equiv \mathbf{R}_\alpha(s^0_\alpha)$ to filament β, we expand the position of filament β off of the z plane, $\mathbf{R}_\beta(s_\beta) \simeq \mathbf{R}^0_\beta + \mathbf{T}\delta s + \kappa\mathbf{N}\delta s^2/2$, where $\delta s = s_\beta - s^0_\beta$, and $\mathbf{T}$, $\mathbf{N}$, and κ are the tangent, normal, and curvature that approximate the local shape of filament β at z (Kamien, 2002). Defining the in-plane separation to be $\Delta \equiv \mathbf{R}^0_\beta - \mathbf{R}^0_\alpha$, the square distance between filament α at z nearby points on β is simply

$$|\mathbf{R}_\beta(s_\beta) - \mathbf{R}^0_\alpha|^2 \simeq |\Delta|^2 + 2\delta s(\mathbf{T}\cdot\Delta) + \delta s^2(1+\kappa\mathbf{N}\cdot\Delta) + O(\delta s^3), \tag{1}$$

which is easily minimized to find the point of nearest contact on β at $\delta s_* \simeq -\mathbf{T}\cdot\Delta/(1+\kappa\mathbf{N}\cdot\Delta)$ and the distance of closest approach

$$\Delta_*^2 = |\Delta|^2 - (\mathbf{T}\cdot\Delta)^2 + O(\Delta^3). \tag{2}$$

Hence, the distance of closest approach between nearby filaments is simply the separation measured perpendicular to the local filament orientation.

In the continuum limit we take tangents to be described by a coarse-grained, continuous field $\mathbf{t}(\mathbf{x})$ such that $\mathbf{T}_\alpha(s) = \mathbf{t}(\mathbf{R}_\alpha(s))$ and consider the square distance of closest approach between infinitesimally spaced filaments $d\Delta = dx\hat{x} + dy\hat{y}$,

$$d\Delta_*^2 = g_{ij}(\mathbf{x})dx_i dx_j, \tag{3}$$

where i and j sum over in-plane directions and we have defined a *metric tensor* to correct for the discrepancy between the distance measured in the plane at z and the plane of interfilament contact

$$g_{ij}(\mathbf{x}) = \delta_{ij} - t_i(\mathbf{x})t_j(\mathbf{x}). \tag{4}$$

The tensor g_{ij} encodes the intuitive effect that interfilament spacing may be altered in two ways: (1) by changing in-plane distance dx_i^2, or (2) by tilting filaments along neighbor directions at constant in-plane spacing, reducing true separation.

By drawing on a formal analogy to the metric geometry of 2D surfaces, we may extend our intuition farther to understand that certain patterns, or textures, of filament orientation geometrically frustrate multifilament packing. Specifically, we may relate the constraints imposed by the interfilament metric, Eq. (4), to a *dual surface* $\mathbf{X}(x,y)$ carrying the same metric $g_{ij} = \partial_i\mathbf{X}\cdot\partial_j\mathbf{X}$ (Millman and Parker, 1977). Here duality implies that geodesic distances measured in this surface are equivalent to the distance of closest approach between corresponding filaments in the packing, and, hence, obstructions to perfect packing of points on $\mathbf{X}(x,y)$ imply corresponding obstructions for filament packing at z.

In particular, it is a classical result of differential geometry, well known to cartographers, that the Gaussian curvature of a surface severely constrains distances between objects defined upon them. The Gaussian, or intrinsic, curvature K of a surface is simply the product of the two principal curvatures κ_1 and κ_2, which are measured along the (orthogonal) directions of locally maximal and minimal curvature (Millman and Parker, 1977). In general, K may be determined directly from the metric and its derivatives, which has the simple approximate form when the deviation from a flat metric (e.g., $g_{ij} = \delta_{ij}$) is small, $K \simeq -(1/2)\epsilon_{ik}\epsilon_{j\ell}\partial_k\partial_\ell g_{ij}$, where ϵ_{ij} is the antisymmetric tensor (Millman and Parker, 1977). This form is sufficient for analyzing the intrinsic geometry of filament packings where tangents are weakly deflected from the z axis.[1] Defining the effective curvature $K_{\rm eff}$ of filament packing at z to be the curvature of the dual surface we find

$$\begin{aligned} K_{\rm eff} &\simeq \tfrac{1}{2}\boldsymbol{\nabla}_\perp \times [\mathbf{t}_\perp(\boldsymbol{\nabla}_\perp \times \mathbf{t}_\perp) - (\mathbf{t}_\perp \times \boldsymbol{\nabla}_\perp)\mathbf{t}_\perp] \\ &= \tfrac{1}{2}[\partial_x^2(t_y)^2 + \partial_y^2(t_x)^2 - 2\partial_x\partial_y(t_x t_y)], \end{aligned} \tag{5}$$

where $\mathbf{t}_\perp$ is the in-plane filament tilt at z and $\boldsymbol{\nabla}_\perp = \hat{x}\partial_x + \hat{y}\partial_y$.

When $K_{\rm eff} \neq 0$ it is impossible for multifilament systems to maintain uniform spacing throughout the packing, just as it is generically impossible to evenly distribute points on 2D surfaces for which $K \neq 0$ (Kléman, 1989; Sadoc and Mosseri, 2008). Hence the operator $K_{\rm eff}$ plays a special role in the geometry of multifilament systems, distinguishing textures that are compatible from those that are incompatible with uniform interfilament spacing. To illustrate the relationship between textures of filament orientation and the dual-surface geometry, we consider two characteristic, radially symmetric patterns of in-plane tilt shown in Fig. 3. A double-twist texture $\mathbf{t}_\perp^{\rm twist} = \Omega(y\hat{x} - x\hat{y})$ corresponds to a *positive* effective curvature $K_{\rm eff}^{\rm twist} = 3\Omega^2 > 0$, consistent with a locally spherical geometry of effective radius $(\sqrt{3}\Omega)^{-1}$. In contrast, for a radial splay texture $\mathbf{t}_\perp^{\rm splay} = \gamma(x\hat{x} + y\hat{y})$ we find a *negative* intrinsic curvature $K_{\rm eff}^{\rm splay} = -\gamma^2 < 0$ consistent with a locally hyperbolic, or saddle, geometry with principle radii of curvature $\pm\gamma^{-1}$. Notice further from Eq. (5) that $K_{\rm eff}$ exhibits a nontrivial dependence on the uniaxial versus biaxial nature of the in-plane texture. For uniaxial (cholesteric) twist textures of equivalent pitch the effective curvature is $1/3$ of the value obtained by a double-twist texture, while $K_{\rm eff} = 0$ for uniaxial (planar) splay.

The implications of "intrinsically curved" filament textures, which we deem as incompatible textures, follow from an application of the famous Gauss-Bonnet theorem (do Carmo, 1976) relating the Gaussian curvature of a surface to geometry of an equilateral triangle connecting three evenly spaced points on $\mathbf{X}(x,y)$ corresponding to centers of three equally spaced neighbor filaments in a packing (see Fig. 4). Assuming the geodesic length of each edge is fixed to the preferred interfilament spacing d the sum of the interior angles θ_v becomes

$$\sum_v \theta_v = \pi + \int_{\rm tri} dA K_{\rm eff}, \tag{6}$$

where the area integral is carried out over the dual-surface patch enclosed by the triangle. Equation (6) shows the well-known result that the sum of interior angles is greater than (less than) π on

[1]The small-tilt form for $K_{\rm eff}$ in Eq. (5) is correct to second order in $\mathbf{t}_\perp$, and is the analog of the small-slope approximation of a 2D surface metric in the Monge gauge where surface geometry is described by surface height $h(\mathbf{x})$ above the x-y plane for which $g_{ij} = \delta_{ij} + \partial_i h\partial_j h$.

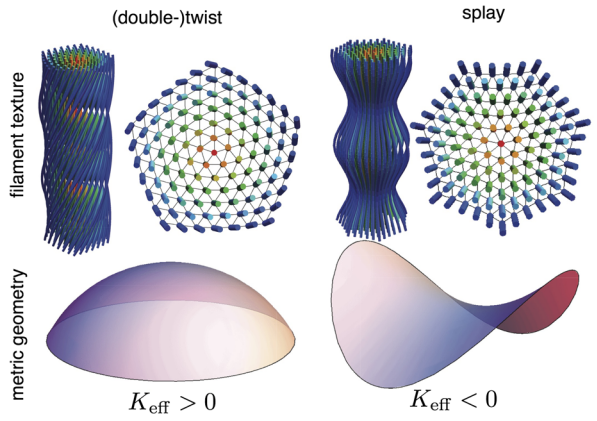

FIG. 3 (color online). Examples of filament textures with positive $K_{\rm eff} > 0$ and negative $K_{\rm eff} < 0$ effective curvatures, whose equivalent surface geometry is shown schematically with spherical and saddlelike surface patches.

surfaces of positive (negative) curvature. Assuming the simplest case for constant $K_{\rm eff}$ within a patch area of $\Delta A_{\rm tri}$, this formula shows that for close packing the interior angle between nearest neighbors becomes $\theta_v = \pi/3 + \Delta A_{\rm tri} K_{\rm eff}/3$. A given filament has 2π of surrounding angle available, from which we construct the *kissing number* Z_k, corresponding to the number of closely packed filaments which can surround a central filament (Rubinstein and Nelson, 1983),

$$Z_k = \frac{6}{1 + \Delta A_{\rm tri} K_{\rm eff}/\pi}. \tag{7}$$

Hence, incompatible textures corresponding to positive or negative effective curvature imply $Z_k < 6$ or $Z_k > 6$, respectively. In general, for $K_{\rm eff} \neq 0$ the close packing is incommensurate with integer values of Z_k, implying that interfilament packing must deviate from constant spacing d and for textures where $K_{\rm eff} \neq 0$ interfilament packing is geometrically frustrated (Sadoc and Mosseri, 2008).

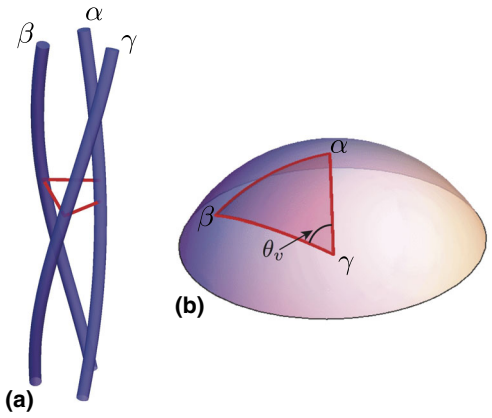

FIG. 4 (color online). (a) A triplet of three twisted filaments, with lines indicating distances of closest approach between them. (b) The mapping of interfilament spacing onto the geodesic separation between three points that form vertices of a geodesic triangle on a positively curved (spherical) surface patch. The Gauss-Bonnet relates the sum of interior angles (labeled as θ_v) to the integrated Gaussian curvature within the triangular patch; see Eq. (6).

The consequence of this geometric frustration is the generation of interfilament or intercolumn stresses for incompatible textures. A physical model for the energetics incompatible textures is based on the continuum elasticity theory of columnar order (Grason, 2010, 2012). Here a free energy functional $F_{\rm col} = \int dV f(u_{ij})$ describes the elastic cost of deformations from a stress-free reference state, where filaments and columns are uniformly parallel and possess long-range 2D lattice order transverse to their orientation, with

$$f(u_{ij}) = \tfrac{1}{2}[\lambda (u_{kk})^2 + 2\mu u_{ij} u_{ij}], \tag{8}$$

where u_{ij} is the 2D strain tensor describing elastic deformations of the columnar lattice (assumed here to be hexagonal) and λ and μ are the Lamé elastic constants parametrizing the cost of deformations of lattice order (Selinger and Bruinsma, 1991). Because columns maintain translational symmetry along their long axis, deformations are described by a two-component displacement field $\mathbf{u}_\perp(\mathbf{x})$, which has components in the 2D plane perpendicular to the reference filament orientation, assumed to be the z axis. Along with 2D positional order, columnar systems possess nematic order associated with the orientations of the columns $\mathbf{t}(\mathbf{x})$ and transverse displacements deform both types of order. Column orientations are locked to displacement via

$$\mathbf{t}(\mathbf{x}) = \frac{\hat{z} + \partial_z \mathbf{u}_\perp}{\sqrt{1 + |\partial_z \mathbf{u}_\perp|^2}} \simeq \hat{z} + \partial_z \mathbf{u}_\perp. \tag{9}$$

In turn, orientations are coupled to intercolumn strains through the strain tensor,

$$u_{ij} \simeq \tfrac{1}{2}(\partial_i u_{\perp j} + \partial_j u_{\perp i} - t_i t_j), \tag{10}$$

where the geometrically nonlinear contribution from in-plane tilt derives from the ability of columnar systems to reduce spacing through pure tilt (Grason, 2012) demonstrated in Eq. (4), and therefore, preserves the rotationally invariant elastic energy (to fourth order in t_i).

The intercolumn stress defined by $\sigma_{ij} = df/du_{ij} = \lambda u_{kk}\delta_{ij} + 2\mu u_{ij}$ is subject to a *compatibility condition* which ensures that stresses are compatible with the definition of strain, the geometry of tilt patterns, and the topology of the displacement field (Grason, 2010). The condition derives formally from evaluating antisymmetric derivatives of strain $\epsilon_{ik}\epsilon_{j\ell}\partial_k\partial_\ell u_{ij}$ (Nelson, 2002),

$$Y^{-1}\nabla_\perp^2 \sigma_{kk} = s(\mathbf{x}) - \boldsymbol{\nabla}_\perp \times \mathbf{b}(\mathbf{x}) - K_{\rm eff}, \tag{11}$$

where $Y = 4\mu(\lambda+\mu)/(\lambda+2\mu)$ is the 2D Young's modulus and $s(\mathbf{x})$ and $\mathbf{b}(\mathbf{x})$ are the respective densities of disclinations and edge dislocations, respectively, in the transverse lattice order.[2] This compatibility relation shows that there are two fundamentally distinct origins of incompatibility in columnar

[2]Considering only the elastic energy, the Euler-Lagrange equation for the displacement is $\partial_j \sigma_{ij} = \partial_z[t_j \sigma_{ij}]$, which strictly speaking also contributes a term proportional to $\partial_z \partial_i [\sigma_{ij} t_j]$ to the right-hand side of Eq. (11).

systems: topological defects described by multivalued configurations of $\mathbf{u}_\perp$ and lattice bond angle, and incompatible orientation textures for which $K_{\text{eff}} \neq 0$. On the one hand, topological defects are singular sources of stress, "quantized" according to the discrete symmetries of the underlying 2D lattice, while the effective curvature K_{eff} varies continuously, in magnitude and spatial distribution, according to the geometry of column orientation. Accordingly, much like 2D crystalline membranes (Nelson and Peliti, 1987; Seung and Nelson, 1988), the effective curvature of columnar and filamentous systems may be viewed as a continuous distribution of disclinations of local topological charge density $-K_{\text{eff}}$ (Kléman, 1989).

In the absence of defects, it is straightforward to determine the energetic costs of incompatible textures. For example, a bundle of lateral size R, Eq. (11) implies intercolumnar stresses of order $\sigma \approx Y K_{\text{eff}} R^2$ whose energetic cost grows as $F_{\text{col}}/V \approx Y(K_{\text{eff}}R^2)^2$ implying the elastic costs of geometric frustration are strongly dependent on system size, becoming prohibitive and potentially self-limiting for finite K_{eff} in the thermodynamic limit of $R \to \infty$ (Grason and Bruinsma, 2007; Grason, 2009). As we show in the next section for twisted bundles, one further consequence of the geometrically induced stresses for large $|K_{\text{eff}}R^2|$ is the stability of topological defects in the ground-state lateral packing of incompatible textures.

III. TOPOLOGICAL DEFECTS IN TWISTED BUNDLES

We next consider the optimal structure and energetics of the twisted filament bundle (Fig. 5). This texture, which for narrow bundles might be recognized as the "double-twist" tube that is the building block of liquid crystal blue phases (Wright and Mermin, 1989), is the simplest example of the nontrivial frustration of interfilament spacing by an incompatible texture. Here filament or column backbones are described by the rigid rotation of in-plane positions about a central axis, say $x = y = 0$ along the pitch axis $\hat{z}$. Filament α in the bundle is described by the helix,

$$\mathbf{R}_\alpha(z) = \mathbf{R}^0_\alpha + \mathbf{R}^0_{\alpha\perp}[\cos(\Omega z) - 1] + (\hat{z} \times \mathbf{R}^0_{\alpha\perp}) \sin(\Omega z) + z\hat{z}, \tag{12}$$

where $\mathbf{R}^0_\alpha$ is the filament position at $z = 0$, $\mathbf{R}^0_{\alpha\perp}$ is the position in the x-y plane at $z = 0$ (i.e., vector separation from the central axis), and $2\pi/\Omega$ is the helical pitch of the bundle, which is constant throughout the bundle. The orientation profile of filaments has the simple form

$$\mathbf{t}(\mathbf{x}) = \cos\theta(\rho)\hat{z} + \sin\theta(\rho)\hat{\phi}, \tag{13}$$

where the local tilt angle with respect to the pitch axis follows

$$\tan\theta(\rho) = \Omega\rho, \tag{14}$$

which goes from $\theta = 0$ at the center to $\theta = \pi/2$ as $\rho \to \infty$ indicating an asymptotic approach to a circular shape for filaments far from the central axis. The application of Eqs. (3) and (4) yields the interfilament metric for a twisted bundle in polar coordinates (ρ, ϕ),

$$d\Delta^2_* = d\rho^2 + \rho^2 \cos^2\theta(\rho) d\phi^2. \tag{15}$$

This metric has a simple and familiar interpretation in terms of an axisymmetric dual surface (Fig. 6), where ρ is the arc distance from the "pole" of the surface and ϕ is the azimuthal angle around that axis (Bruss and Grason, 2012). The length of a "latitude" $\ell(\rho)$ that encircles the pole a distance ρ is simply

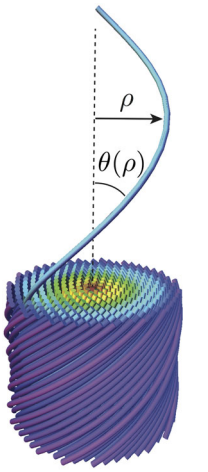

FIG. 5 (color online). A (double-)twisted bundle, where the color gradient highlights the radial distance of filaments from the central filament. A single, helical filament is shown in the upper portion to highlight the local tilt angle $\theta(\rho)$ between the filament at radius ρ and the pitch axis.

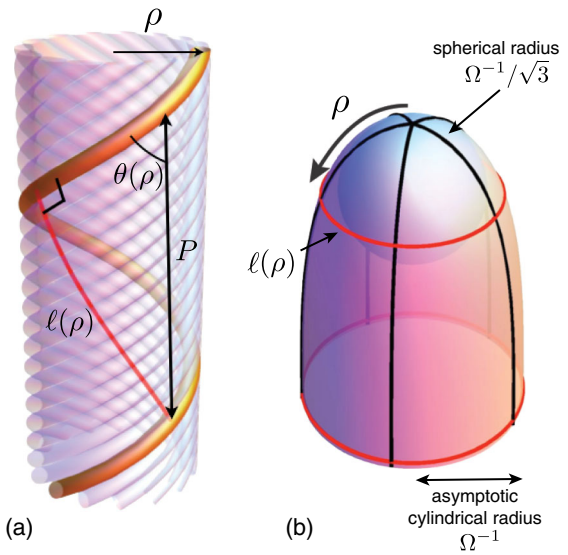

FIG. 6 (color online). (a) The packing of finite-diameter filaments at a radial distance ρ from the bundle center. The amount of space available for packing filaments at ρ is determined by the length $\ell(\rho)$ of a curve between to two points of "self-contact" along the same filament. (b) The 2D axisymmetric surface that carries the interfilament metric properties of a twisted bundle. The lines of latitude of length $\ell(\rho)$ as defined by the geometry in (a).

$$\ell(\rho) = 2\pi\rho\cos\theta(\rho) = P\sin\theta(\rho), \tag{16}$$

where we used $2\pi/P = \Omega$.

In a twisted bundle $\ell(\rho) = 2\pi\rho/\sqrt{1+(\Omega\rho)^2}$ can be understood by considering the space available for filaments a radial distance ρ from the center. The maximum number of filaments that can be placed at ρ is constrained by the length of a curve that passes perpendicular to filaments between two points of contact along the same helical filament [see Fig. 6(a)]. In recent studies of closed-packed, n-ply geometries (Neukrich and van der Heijden, 2002; Olsen and Bohr, 2010), in which n filament are packed a fixed radius ρ_p from the central twist axis of a ply, the nonlinear ρ dependence of $\ell(\rho)$ has been implicated in a surprising "geometrical jamming" behavior. The constraints on nonoverlap imply a distance between neighbor filaments d, a condition which we may approximate at large n by $d \simeq \ell(\rho_p)/n$, and, therefore, requires that ρ_p increase with twist as $\rho_p \simeq d/\sqrt{(2\pi/n)^2 - (\Omega d)^2}$. The filament length per turn of the ply is $L_t(\Omega) = 2\pi\Omega^{-1}\sqrt{1+(\Omega\rho_p)^2}$, which when combined with divergence of ρ_p at a finite twist $(\Omega \to 2\pi/nd)$ implies that the number of turns for fixed-length filaments is a nonmonotonic function of Ω (Olsen and Bohr, 2011). That is, n plies achieve a maximum number of turns at a finite twist for which $dL_t^{-1}/d\Omega = 0$, a purely geometric phenomenon which we may now relate to the packing of disks on an axisymmetric curved surface.

Given the axisymmetry of the metric in Eq. (15), it is straightforward to reconstruct an axisymmetric surface in 3D that encodes the metric properties of the twisted bundle. Specifically, adopting cylindrical coordinates where $\hat{r}_\perp = \cos\phi\hat{x} + \sin\phi\hat{y}$, the surface has the form

$$\mathbf{X}(\rho,\phi) = \frac{\ell(\rho)}{2\pi}\hat{r}_\perp + z(\rho)\hat{z}, \tag{17}$$

where the function $z(\rho)$ satisfies

$$\frac{\partial z}{\partial\rho} = \pm\sqrt{1-\cos^6\theta(\rho)}, \tag{18}$$

and we used $(2\pi)^{-1}\partial\ell/\partial\rho = \cos^3\theta(\rho)$. This surface shown in Fig. 6(b) has a tapered, silolike geometry characterized by the distribution of Gaussian curvature which follows directly from derivatives of the metric (Millman and Parker, 1977),

$$K_{\text{eff}} = -\frac{1}{2\ell(\rho)}\frac{\partial^2\ell(\rho)}{\partial\rho^2} = 3\Omega^2\cos^4\theta(\rho). \tag{19}$$

This exact form of the curvature distribution agrees with the "small-tilt" calculation described in the previous section only at the center of the bundle where $K_{\text{eff}}(\rho\to 0) = 3\Omega^2$ where the geometry of the dual surface is locally well approximated by the sphere of radius $\Omega^{-1}/\sqrt{3}$. In the large-tilt regime corresponding to points far from the bundle center where $\Omega\rho \gg 1$, the intrinsic curvature vanishes as $K_{\text{eff}}(\rho \gg \Omega^{-1}) \simeq 3\Omega^{-2}\rho^{-4}$, indicating an asymptotic approach to a cylindrical geometry for the dual surface. The concentration of Gaussian curvature at the pole of the dual surface implies frustration of interfilament packing is largely localized to within a radial distance of order P from the center of the bundle, while sufficiently far from the bundle center, metric constraints permit a nearly regular interfilament spacing, asymptotically commensurate with hexagonal packing, i.e., $Z_k(\rho\to\infty)\to 6$ (Bruss and Grason, 2012).

It is important to recognize that the notion of metric equivalence between twisted bundles and the dual surface is not restricted to the limit of infinitesimally spaced filaments. That is, the closest distance between any two helical curves in the bundle is identical to the geodesic distance measured between equivalent points on the surface, no matter the separation.[3] This is important because it implies that the duality between the problems of packing in twisted bundles and packing on the dual surfaces holds for finite-sized elements. For example, we may consider steric, hard tube interactions to prevent interfilament separations smaller than a diameter d. The duality between packing in bundles and on the dual surface implies that any nonoverlapping configurations of (geodesic) disks of diameter d on the surface correspond one to one to three-dimensional configurations of nonoverlapping filaments of diameter d in the bundle [see, e.g., close-packed twisted bundles in Bruss and Grason (2012)].

The equivalence between discrete packings of finite-diameter elements provides a useful way to illustrate and understand the metric equivalence between bundles and their dual surfaces. Consider a horizontal section of a twisted bundle as shown in Figs. 7(a) and 7(b) and note the apparent "warping" of the circular cross sections of the helical tubes in the sections: horizontal slices of filaments near the bundle center remain circular due to the normal intersection with a horizontal plane, while slices toward the outer edge of the bundle stretch, or warp, azimuthally due to the increased tilt. Consider also the equivalent disk packing on the dual surface shown in Fig. 7(c). Because of the nonzero Gaussian curvature of the dual surface, any projection of the disk packing to a planar surface will distort the image of the disk packing with a local geometry that varies throughout the projected image, familiar from continental distortions in cartographic projections of the globe to flat maps (Bugayevsky and Snyder, 1995). See, for example, the disk packing in orthographic projection [i.e., viewed from above in Fig. 7(d)], where disks appear compressed along the radial directions away from the pole at the center of the image. Viewed from another

[3]This follows from the fact that any curve C_{12} between two points (ρ_1,ϕ_1) and (ρ_2,ϕ_2) on the dual surface maps onto a unique three-dimensional curve C'_{12} in the bundle that connects filaments at (ρ_1,ϕ_1,z_0) and (ρ_2,ϕ_2,z_0) and that intersects all intervening helical curves perpendicular to their backbones. Further, metric equivalence between the surface bundle implies these curves share the identical length (i.e., $L_{C_{12}} = L_{C'_{12}}$). Likewise, any curve in the bundle maps onto a unique, equal-length curve on the surface. Consider the geodesic path G_{12} between two end points on the surface, which maps to curve G'_{12} in the bundle with $L_{G_{12}} = L_{G'_{12}}$. Because the length of any other curve C_{12} between the same end points must have $L_{C_{12}} \geq L_{G_{12}}$, it follows that G'_{12} must also be the shortest possible path between end point filaments in the bundle (i.e., a straight line connecting points of contact).

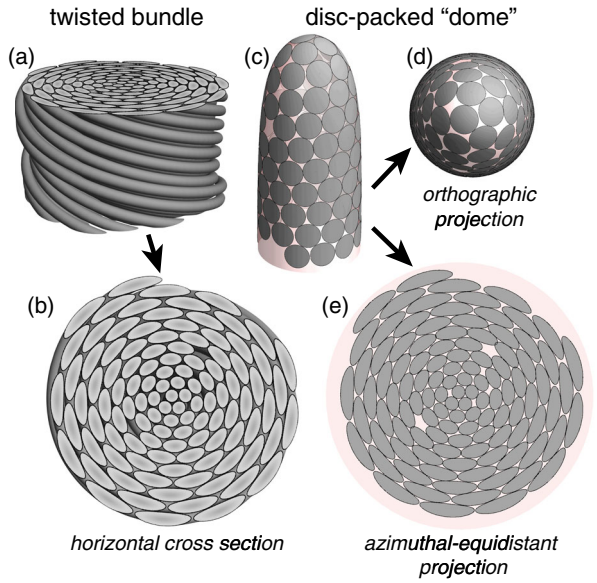

FIG. 7 (color online). Equivalence of finite-diameter filament packing in twisted bundles, and finite-diameter disk packing on a "domelike" surface carrying the metric of a twisted bundle. (a) The side view and (b) the top view of a twisted bundle, highlighting noncircular shapes of the filament intersections with the plane perpendicular to the pitch axis. (c) A side view of the equivalent disk packing on the "dome" shown in Fig. 6(b), and (d), (e) two "polar" projections of the disk packing. The orthographic projection in (d), a view from the top down, preserves distances along the azimuthal direction while compressing distances along the radial direction. (e) The azimuthal equidistant projection preserves radial distances while stretching azithumal distances, producing the identical image of the filament intersections (azimuthally stretched disks) shown in (b).

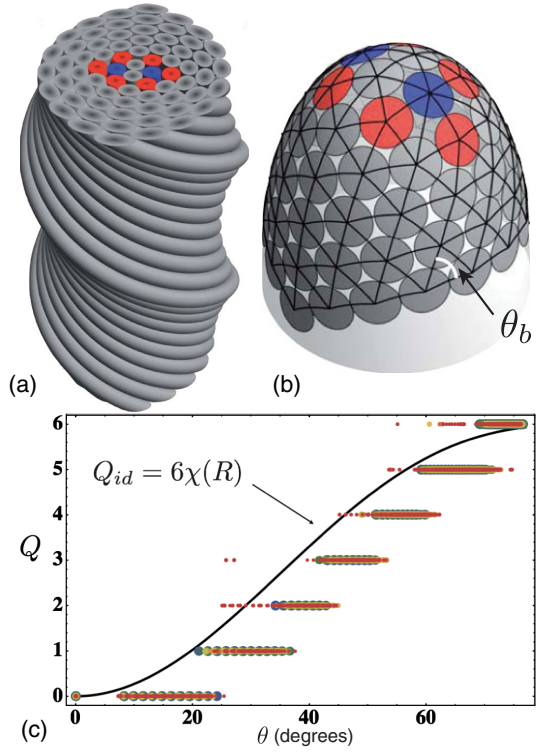

FIG. 8 (color online). A simulated ground state of an $N = 70$ twisted bundle from Bruss and Grason (2012) is shown in side view in (a), along with the corresponding disk packing on the bundle-equivalent surface in (b). Triangulation of the packing on the curved surface yields the nearest-neighbor "bond network," identifying defects in the packing as deviations from sixfold coordination of the bond network (i.e., disclinations). Filaments with fivefold, sixfold, and sevenfold neighbor coordination are highlighted in different shades. (c) The total topological charge of the ground-state packing Q, defined in Eq. (20), plotted as a function of the twist angle of the outermost filament in the bundle $\theta = \arctan(\Omega R)$ with the colored data points showing results from simulated ground states and the solid line showing the geometric prediction for the ideal topological charge given by Eq. (24).

projection which maintains distances measured from the $\rho = 0$ pole [see Fig. 7(e)] known as the *azimuthal equidistant* projection, we find that the projected image of dual-surface disk packing is identical to images of the planar section of bundle normal to the pitch. Other planar sections of the bundle, those not necessarily normal to the pitch axis, correspond to azimuthal equidistant projections of the same disk packing where the center of the image is no longer a point of axial symmetry of the dual surface (the pole at $\rho = 0$). The warping of filament sections in the planar cut of a bundle has long been recognized in the context of the so-called "contact" problem in textiles and yarns (Hearle, Grosberg, and Backer, 1969; Pan and Brookstein, 2002), although only recently has the connection to non-Euclidean geometry been understood.

A. Disclinations in twisted bundles

The non-Euclidean metric geometry and the associated global and local constraints on interfilament packing implied by the mapping have critical consequences for physical models of cohesive filament assembly in twisted bundles. The Gauss-Bonnet theorem and its application to triangulations of disk packings on the dual surface may be exploited to derive the relationship between bundle twist, the topology of the nearest-neighbor bond network in the bundle, and the deformation of ideal interfilament geometry (Bruss and Grason, 2012). Figure 8 shows a filament bundle and its dual representation as a curved-surface disk packing. Because the geodesic distances measured on the surface represent the true interfilament spacing, the triangulated network of nearest-neighbor bonds on the surface properly encodes the topology of nearest interfilament contact. In particular, from the triangulation of the dual packing we may count the neighbor statistics of filaments in the packing, and its deviation from the sixfold packing of a parallel bundle. Denoting the number of filaments (or disks) in the bulk of the bundle (not a surface vertex) possessing n neighbor bonds by V_n, we define the total topological charge of the bundle to be

$$Q = \sum_n (6 - n) V_n. \tag{20}$$

This definition is consistent with the definition of topological *disclination* charge where points of fivefold (sevenfold) coordination in the bond network correspond to $+1$ (-1)

contributions to Q (Nelson, 2002). Applying Eq. (6) by summing over the triangulated faces of nearest-neighbor mesh and using the facts that (1) each face is spanned by three edges (or "bonds"), (2) each edge connects two vertices, and (3) each internal (nonsurface) vertex accounts for 2π total internal angle, we arrive at a generalized version of the Euler-Poincaré formula (Kamien, 2002)

$$Q - 6\chi = N_b\langle\delta\theta_b\rangle, \tag{21}$$

where

$$\chi = \frac{1}{2\pi}\int_{\text{mesh}} dA K_G \tag{22}$$

quantifies the total integrated Gaussian curvature within the triangulated packing and the right-hand side describes the N_b internal angles of boundary vertices θ_b from equilateral packing with

$$\langle\delta\theta_b\rangle = \frac{1}{N_b}\sum_b(\theta_b - \pi/3), \tag{23}$$

where θ_b is shown schematically in Fig. 8(b).

Typical applications of the Euler-Poincaré formula consider triangulations without boundary (say, for crystalline packings on surfaces of spherical topology), such that the right-hand side is zero ($N_b = 0$) and Q is a topological invariant, fixed by the Euler characteristic χ (Bowick and Giomi, 2009). In the case of a twisted bundle, the total disclination charge is not a topological invariant,[4] and the deficit between Q and 6χ will be accommodated by packing deformation at the boundary (i.e., $\langle\delta\theta_b\rangle \neq 0$). Nevertheless, Eq. (21) provides a useful heuristic for understanding the structure of low-energy packings by noting that the right-hand side a measure of the interfilament strain in the packing. Intuitively, one expects that interactions that favor equidistant filaments will favor equilateral packing at the boundary (specifically in the limit of $d \to 0$ where area per face vanishes); hence, $\langle\delta\theta_b\rangle \neq 0$ indicates a locally suboptimal geometry. More specifically, the magnitude of interfilament strain, or the variation of interfilament spacing, implied by $\langle\delta\theta_b\rangle \neq 0$ can be understood in terms of the mean geodesic curvature $\kappa_g \approx 3\langle\delta\theta_b\rangle/d$ of lattice row in a nearly triangular packing of average spacing d. Because of the row curvature, the change in spacing between successive rows is roughly $\kappa_g d^2$. For a bundle with a number of radial rows N_r, the relative change of spacing between filaments at the center and periphery of the bundle, respectively, d_0 and d_b, becomes $d_b/d_0 - 1 \approx N_r\langle\delta\theta_b\rangle$. For 2D bundles where $N_r \propto N_b$, it follows from Eq. (21) that $Q - 6\chi$ is indeed proportional to the excess separation between filaments at the bundle surface relative to the center.

As cohesive interactions favor uniform interfilament spacing throughout, a simple conjecture is that in *energy-minimizing bundles* the packing prefers values of topological charge where $\langle\delta\theta_b\rangle = 0$, such that the ideal topological charge may be defined as $Q_{id} \equiv 6\chi$. Assuming that bundle cross sections retain a roughly circular shape, we may calculate the dependence of Q_{id} on the twist and radius of bundles,

$$Q_{id} = \frac{3}{\pi}\int d\rho\ell(\rho)K_{\text{eff}}(\rho) = 6[1 - \cos^3\theta(R)], \tag{24}$$

where we use $dA = d\rho\ell(\rho)$ and Eq. (19). This simple relationship makes three significant predictions about the optimal (energy-minimizing) packing of twisted bundles. First, the preferred disclination charge of bundles is independent of filament diameter, depending only on the tilt angle θ at the surface of the bundle, which itself is fully determined by the ratio R/P. Second, for $\theta \neq 0$, $Q_{id} \geq 0$, indicating a preference for excess fivefold coordinated ($Q = +1$) sites in the bundle cross section. Third, the preferred topological charge of the packing increases from $Q_{id} = 0$ at $\theta = 0$ to a maximum of $Q_{id} = 6$ as $\theta \to \pi/2$.

These predictions for the optimal distribution of defects in the cross section of twisted filament bundles have been tested in the context of numerical simulations of cohesive filament bundles (Bruss and Grason, 2012, 2013). The simulations employ a simple stochastic algorithm to optimize the cohesive energy of an N-filament bundle with fixed twist Ω. Here the finite-diameter d of filaments enters as the energy minimum of pairwise cohesive interactions, which was assumed to have a form similar to a Leonard-Jones potential in which the separation is the distance of closest approach between helical center lines of filaments. Figure 8(c) compares the Q_{id} to the topological charge Q of numerically minimized bundle packings for $N = 16 - 196$, which is extracted directly from triangulated neighbor packing that has been conformally mapped to the plane. Notwithstanding its continuous θ dependence as well as the simple assumption of cylindrical bundle shape, the form of Q_{id} in Eq. (24) does a remarkable job of capturing the increase in the excess of fivefold defects of numerical ground-state packings.

As shown in Fig. 9(b), which maps the minimal-energy value of Q in terms of θ and N, these simulations confirm that the net topological charge is solely determined by the twist angle (or equivalently by the integrated curvature on the dual surface) and independent of the filament number. The evidently universal dependence of Q on θ is all the more surprising when analyzing the dependence of other structural measures of the packing on θ and N. For example, in Fig. 9(c) we show the total number of disclinations per topological charge Q (where disclination here refers to any non-six-fold coordinated filament in the bulk packing), which unlike Q itself exhibits a complex and nonuniversal dependence on both filament number and bundle twist, highlighting N-dependent transitions between multiple ground-state defect

[4]Equations (20)–(23) restrict the analyses to "internal" or "nonboundary" disclinations. Although it is possible to consider disclinations defined on the open boundary of a 2D bond network (Bowick and Giomi, 2009), such "defects" do not generate the far-field elastic strains of an intervertex position favored by Gaussian curvature. Although the sum of internal and "boundary" disclinations is always 6 for any effective curvature (twist), due to distinct geometric influence of these two different populations, the distribution of these defects in the ground state shifts from boundary-only defects in untwisted bundles to predominantly or exclusively internal defects in highly twisted bundles.

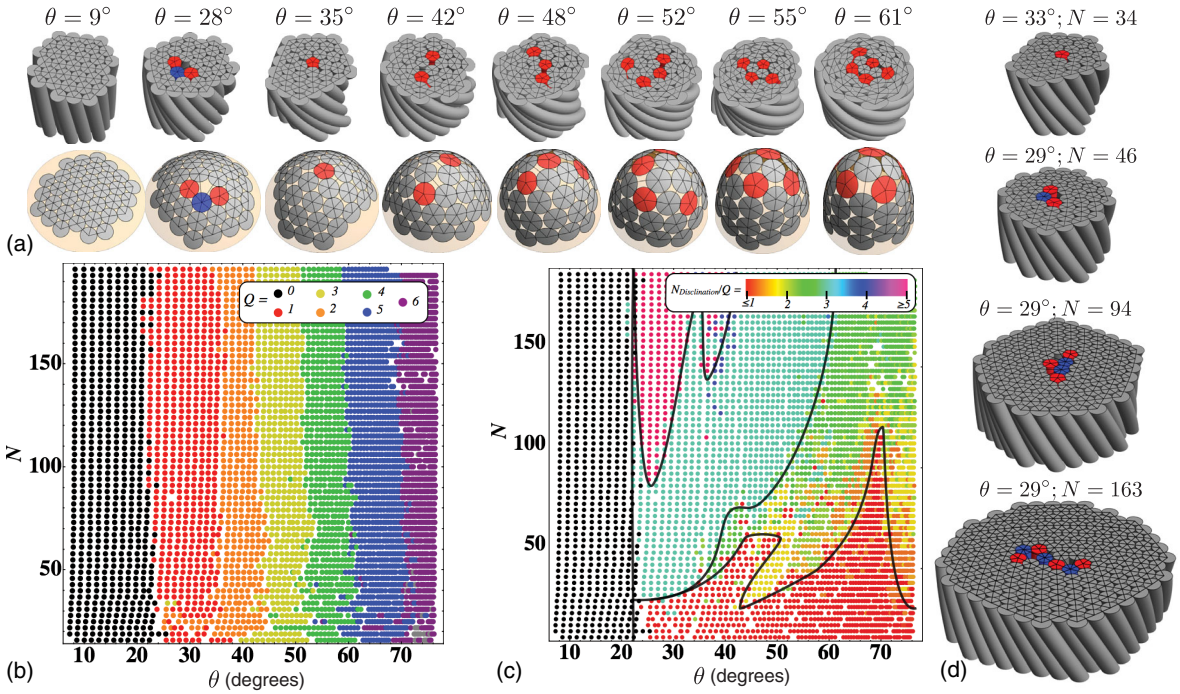

FIG. 9 (color online). Simulated ground states of twisted filament bundles. (a) Optimal packings of a 34-filament bundle, with increasing twist angle showing an increase in the number of fivefold (disclination) defects. (b) The total topological charge of simulated ground states for bundles of variable twist angle $\theta = \arctan(\Omega R)$ and filament number N. (c) The number of disclinations per charge $N_{\text{disclination}}/Q$ is shown for simulated ground states, with dark lines drawn to guide the eye to regions of roughly constant value. (d) A series of simulated ground states at fixed $\theta \approx 30°$ (corresponding to $Q = 1$) with increasing N, showing the transition from compact disclinations to extended "charged scars" of alternating 5–7 defect pairs. Adapted from Bruss and Grason, 2012, 2013.

patterns. One critical observation is the abundance of an excess 5–7 pairs in the energy-minimizing states of large-N bundles [Fig. 9(d)], a trend which is not unlike the formation of "grain boundary scars" on spherical (Bowick, Nelson, and Travesset, 2000; Bausch *et al.*, 2003) and catenary (Irvine, Vitelli, and Chaikin, 2010) surfaces at large N.

Despite these obvious complexities in the detailed ground-state structure (in numbers, positions, and charge of individual defects), optimal bundles maintain a fixed and universal value of a net number of fivefold defects as measured by Q for a given θ consistent with the purely geometric considerations implied by the dual-surface mapping. The universal evolution of Q with twist implies a corresponding universality in the θ dependence of the energy of the bundle. Figure 10(a) shows the plots of E_{bulk}/V "bulk" energy density (total surface filament energy) versus θ for simulated ground states in the range of N. Again, despite the differences in the detailed packing structure, for large N the bulk energy shows a characteristic dependence on θ that is dominated in the underlying and universal changes in Q. At low angle, the energy of a defect-free ($Q = 0$) bundle exhibits a roughly power-law increase with θ. The monotonic θ dependence holds until a critical value of $\theta_{\text{disc}} \simeq 25°$, at which point the ground state becomes unstable to an excess fivefold defect, $Q = 1$, marked by a cusp and secondary minimum, indicating the mitigating effects of defects in highly twisted bundles. Further cusps appear on the transitions to higher integer Q, leading a characteristic "sawtooth" dependence of E_{bulk}/V on θ in the defect-mediated regime. Notably, an energetic landscape of similar structure was calculated in the context of continuum elasticity theory calculations of twisted bundles (Grason, 2010, 2012) possessing energy-minimizing configurations of fivefold disclinations [Fig. 10(b)]. At small twist, predictions of the continuum theory appear quantitatively consistent for small twist [notably, continuum theory predicts a critical angle of $\theta_{\text{disc}} = \arctan(\sqrt{2/9}) \simeq 25.2°$ in good agreement with simulations]. It should be noted that the small-tilt approximation underlying this theory lead to qualitative failures at large twist, including an unbounded increase in Q as $\theta \to \pi/2$.

B. Dislocations in large-N bundles

Fivefold disclinations are evidently favorable in sufficiently twisted bundles, yet these topologically charged defects are not the only means of relaxing geometrical frustration in bundles. Indeed, for sufficiently large bundles ($N \gg 1$) excess disclinations which appear only above a critical threshold of twist $\theta_{\text{disc}} \simeq 25°$ are preempted by a class of topologically neutral defects that become stable at lower twist (Azadi and Grason, 2012). These defects, edge dislocations in the cross section, are "bound" 5–7 pairs (Nelson, 2002), which correspond to a partial row of filament positions that terminates within the bulk of the packing. Because these defects are energetically stable only at sufficiently large N, dislocation-only ground states of twisted bundles have not been characterized via the numerical methods applied for stable disclination patterns for $N \lesssim 200$. Nonetheless, the regime of

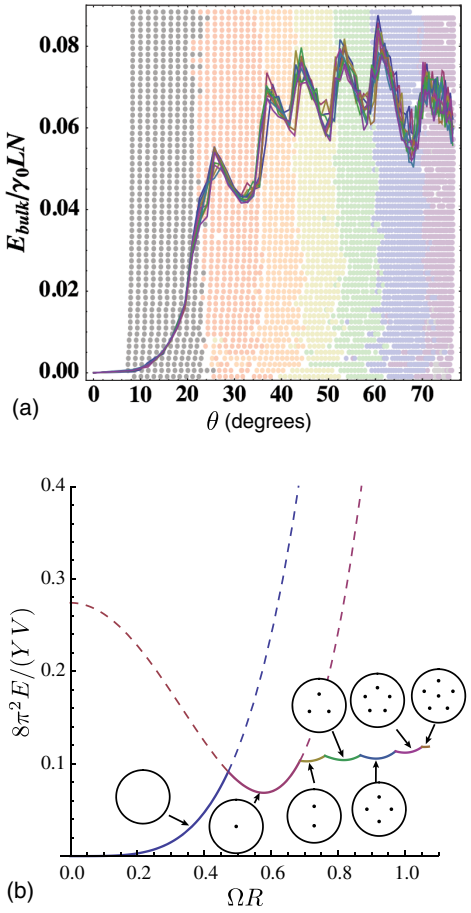

FIG. 10 (color online). (a) The bulk energy density (total energy minus excess energy of surface filaments) of simulated ground states of twisted bundles vs twist angle, for large bundle sizes $N = 166 - 193$ as computed by Bruss and Grason (2013). Energy curves are overlaying the results for Q, highlighting the coincidence of multiple minima in the energy density with stepwise transitions in an optimal value of Q. (b) The shape of the simulated bulk energy density is compared to continuum elasticity theory calculations for twisted bundles possessing only fivefold disclinations, calculated by Grason (2010, 2012), with optimal arrangement of defects shown for each distinct branch (corresponding to distinct Q values) of energy minimal. The dashed lines show the metastable branches of defect-free and $Q = 1$ elastic energy density, which meet at the transition point $(\Omega R)_{\rm disc} = \sqrt{2/9}$ (corresponding to $\theta_{\rm disc} \simeq 25°$).

large bundle size $R/d \gg 1$ and low-twist $\theta \ll 1$ where multidislocation patterns emerge as minimal-energy configurations is well suited to the continuum elastic theory of 2D ordered bundles outlined in Sec. III.A.

The stability of dislocations can be understood by considering the stress distribution in a defect-free twisted bundle and the work done to remove a partial row of filament positions in the bundle, to create an edge dislocation (Azadi and Grason, 2012). The dominant contribution to the stress derives from the tilt-induced azimuthal compression of interfilament spacing at the outer periphery of the bundle, from which we can crudely estimate the magnitude of this stress as $\sigma_{\phi\phi} \approx -Yt_\phi^2 = -Y(\Omega\rho)^2$. A more careful calculation shows that the stress profile of the defect-free state $\sigma_{\phi\phi} = 3Y\Omega^2/128(R^2 - 3\rho^2)$ is only compressive sufficiently far from the bundle core ($\rho \geq R/\sqrt{3}$) (Grason, 2012). To maximize the energy relaxation upon introducing a dislocation, we may consider a Volterra construction (Chaikin and Lubensky, 1995), in which dislocations correspond to the removal of a material along a cut in the bundle cross section. Because of the compressive stress at the bundle periphery, stable dislocations have polarizations corresponding to a Burgers vectors locally aligned to the azimuthal direction and the removal of a partial row of filament positions extending radially from the dislocation (at $\rho \lesssim R$) to the free edge of the bundle. Following standard arguments (Peach and Koehler, 1950), removing a row of filament positions of width $b \simeq d$ and of length $\ell \approx R$ corresponds to a relaxation of the elastic energy by roughly $\sigma_{\phi\phi} dR$, from which we estimate the energy of twist-dislocation coupling $E_{\rm twist}$ to be

$$E_{\rm twist} \approx -Yb\Omega^2 R^3. \tag{25}$$

Comparing this to the elastic self-energy of introducing a single dislocation in the cross section $E_{\rm disc} \approx Yb^2 \ln(R/b)$ (Chaikin and Lubensky, 1995), we estimate the critical degree of bundle twist at which dislocations become stable,

$$(\Omega R)^2_{\rm disl} \approx \frac{b}{R}\ln(R/b). \tag{26}$$

Significantly, while the stability condition of isolated disclinations is predicted to be independent of bundle size [i.e., $(\Omega R)_{\rm disc} = \sqrt{2/9}$] the threshold twist for appropriately polarized dislocations is (1) highly dependent on R/d and (2) found to decrease with increasing bundle size, vanishing in the $R/b \to \infty$ limit. Notably, an essentially equivalent argument was first developed in the context of "neutral" dislocation patterns formed in 2D crystalline assemblies on curved surfaces with open boundaries by Irvine, Vitelli, and Chaikin (2010), yielding a similar increase in dislocation stability as the ratio of crystal size to lattice spacing grows.

A more careful analysis of the position dependence of the elastic energy of dislocations in twisted bundles yields the defect stability diagram shown Fig. 11(a). For sufficiently, narrow bundles $R/b \lesssim 3$ the dislocations and disclinations are predicted to become energetically preferable at roughly the same degree of large twist, comparable to $(\Omega R)_{\rm disc} = \sqrt{2/9}$. In contrast, for mesoscopically large bundles where $R/b \gg 1$ dislocations become stable in twisted bundles at degrees of twist far below the threshold for excess fivefold disclinations, predicting a broad range of multidislocation ground states at intermediate twist for large bundles. To put this into context, we compare these thresholds with the observed size and twist angles of self-twisting filament assemblies. For example, fibrin bundles (Weisel, Nagawami, and Makowski, 1987) and twisted collagen fibrils (Wess, 2008) are observed to have twisted angles in the ranges of 8°–10° and 15°–17°, respectively, which are both well below the threshold angle for stabilization of a single fivefold disclination $\theta_{\rm disc} \simeq 25°$. For bundles of mesoscopic dimensions typical for fibrin and collagen $R \approx 100d$, the elastic theory predicts that dislocations become favorable above a threshold twist of

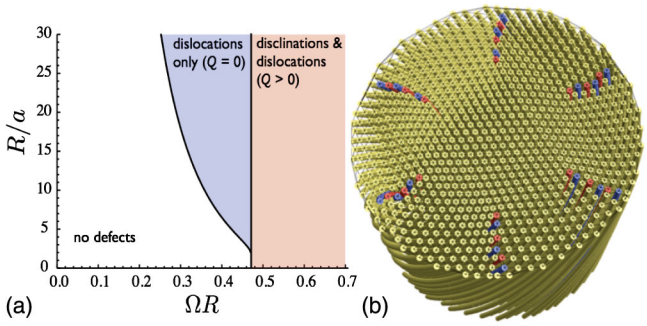

FIG. 11 (color online). (a) Stability phase diagram for defects in twisted bundles, calculated from continuum elasticity theory (Azadi and Grason, 2012), showing regions where dislocations (neutral 5–7 disclination pairs) and charged defect configurations possessing at least one excess fivefold disclination are stable relative to the defect-free bundle. Here a is the interfilament lattice spacing. (b) The "scarred," multidislocation ground state at intermediate twist for sufficiently large bundles (i.e., $R/a \gg 1$), with fivefold and sevenfold coordinated filaments.

$\theta_{\mathrm{disl}}(R/b = 100) \simeq 9°$, below or comparable to the observed twists of either structure. These observations suggest that while excess disclinations may not be stable in some of the most commonly observed twisted filament architectures, stable dislocations and multidislocation patterns are likely features of optimal packing of these materials.

The structure and thermodynamics of multidislocation ground states of twisted bundles was studied using the Green's functions for dislocation sources of stress in cylindrical bundles to calculate the elastic energy of competing defect patterns (Azadi and Grason, 2012). For a bundle twist in excess of the critical dislocation twist $(\Omega R)_{\mathrm{disl}}$, the energetically preferred number of dislocations follows a characteristic scaling with bundle twist and size [see Fig. 12(a)]. This scaling can be understood in largely geometric terms by balancing the length of azimuthal compression at the free boundary on the dual surface $|\ell(R) - 2\pi R| \approx R(\Omega R)^2$ with the azimuthal length $N_d b$ removed by N_d radial lattice rows of width b removed from the periphery of the bundle, yielding

$$N_d \sim \frac{R}{b}(\Omega R)^2. \tag{27}$$

The optimal symmetries of multidislocation patterns have also been explored in the context of ground states of twisted bundles, and, more recently, the context of the dual problem of crystalline "caps" on spherical surfaces (Grason and Davidovitch, 2013; Azadi and Grason, 2014). For $N_d \gg 1$, minimal-energy patterns of dislocations are shown to be radial chains of dislocations, or "neutral scars," extending from the free edge and terminating the bulk of a bundle [see Fig. 11(b)]. This motif of a neutral 5–7 disclination chain, originally dubbed "pleats" when observed in colloidal assemblies on curved 2D surfaces (Irvine, Vitelli, and Chaikin, 2010), has the structure along its length of a tilt-grain boundary separating two orientationally mismatched regions by an angle $\delta\phi \simeq b/D$, where D is the spacing between dislocations along the scar. While an ordinary grain boundary does not terminate

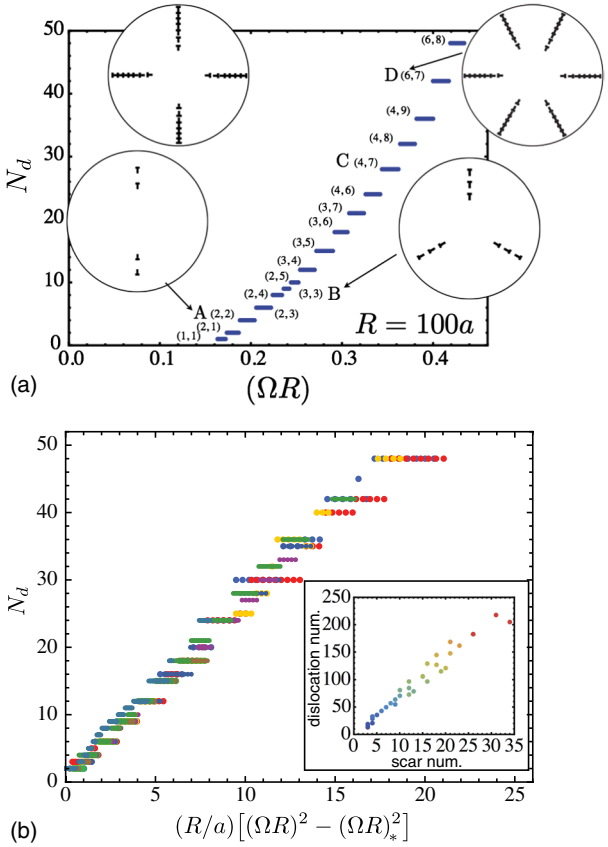

FIG. 12 (color online). (a) Optimal number of dislocations vs bundle twist in a $R = 100a$ bundle, from continuum theory of twisted bundles (Azadi and Grason, 2012). The integer pair (m, n) refers to structures with m "scars" each possessing n dislocations. (b) The collapse of the total number of defects (from bundles $R/a = 20 - 700$) with parameter $R/a[(\Omega R)^2 - (\Omega R)_*^2]$ where $(\Omega R)_*$ is the critical twist for stable dislocations. The inset of (b) shows the proportionality between the total dislocation number and optimal scar number, roughly predicting six dislocations per scar independent of R/a. Here the color scale indicates the gradient in bundle sizes corresponding to large and smaller R/a, respectively.

in the bulk of the crystal, the "tips" of scars do, and, therefore, act as singular, disclinationlike points around which the lattice orientation rotates rapidly by $\delta\phi$. It was recently shown (Azadi and Grason, 2014) that the elastic competition between these distinct portions of scars—on the one hand, the "line tension" of the scars which prefers to localize dislocations into a small number of high-angle grain boundaries and, on the other hand, the disclinationlike tips of scars which alternatively favor a larger number of small-angle grain boundaries—selects an optimal number of scars $n_s \sim N_d$ which diverges in direct proportion to the number of dislocations as $R/b \to \infty$. Figure 12(b) shows the linear relationship between N_d and n_s for simulated ground-state patterns of dislocations of bundle sizes in the range of $R/b = 20 - 700$. Remarkably, these results predict that the ratio N_d/n_s, the number of dislocations per scar, approaches a universal value [≈6 from the slope of N_d vs n_s in Fig. 12(b)], independent of lattice spacing, bundle twist, or other materials parameter in the asymptotic limit $R/b \to \infty$.

IV. TWISTED TORI IN CURVED (AND FLAT) SPACE

In this section we review geometrical approaches to the problem of twisted filament packing based on studies of *fibrations* of the 3-sphere (S^3). As was first understood in the context of curved-space models of the liquid crystal blue phases, the ambient positive curvature of S^3 admits uniform double-twist textures which are otherwise frustrated in Euclidean space (R^3) (Sethna, Wright, and Mermin, 1983). This fact provides a means to construct and study ideal twisted structures in curved space whose structure becomes heterogeneous, perhaps defect riddled, upon projection to R^3.

A second important feature of the twisted fibrations of S^3, particularly their projections to R^3, is that they provide a natural means to construct twisted toroidal bundles. Similar to the straight bundles of the previous section, in twisted toroidal bundles filament positions rotate around a central backbone along its contour, but unlike straight bundles, twisted toroids have backbones that also bend around into a closed curve. Toroidal assemblies of filaments and columns are known to form in a variety of systems (e.g., condensed DNA, collagen, and columnar droplets), and, therefore, a generic model of structure and thermodynamics of interfilament packing in this geometry has broad value. Beyond its potential application to any of these material systems, the physical and geometric theory of packing in twisted toroidal bundles provides a natural way to analyze the interplay between bundle geometry and interfilament organization, beyond straight, twisted bundles. Simply put, how are the metric properties and consequences thereof altered when a filament bundle is twisted and simultaneously *bent*?

In the context of liquid crystalline materials, the unique geometry of textures in S^3 first drew interest as a conceptual approach to "defrustrating" double-twist textures which are characteristic of chiral, blue phases (Wright and Mermin, 1989). Kléman (1985) was the first to consider how metric properties of ideal fibrations (that is, properties beyond orientation) would be relevant to physical models of twisted filament packing, albeit, filaments embedded in an unphysically curved space. More recently, Charvolin and Sadoc (2008) and Sadoc and Charvolin (2009) expanded on this initial analysis by exploring a more general class of fibrations and their projections to twisted toroidal bundles in R^3. In this section, we aim to provide primarily a descriptive summary of the key properties of twisted filament packing geometry in S^3, metric features of their projections to R^3, and the connection to the twisted, straight bundle packing problem of the previous Sec. III. An interested reader will find considerably more detailed analyses of 3-sphere fibrations in Sadoc and Charvolin (2009).

A. Double-twisted filament packings in S^3

S^3 can be constructed as a three-dimensional submanifold of a four-dimensional (Euclidean) space satisfying

$$x_1^2 + x_2^2 + x_3^2 + x_4^2 = \Omega^{-2}, \tag{28}$$

where Ω^{-1} is the radius of the 3-sphere, which can be related to a twist of embedded filament packings. Critical to models of filament packing is the structure of fibrations of S^3 (Sadoc and Mosseri, 2008), which are decompositions of this space into a collection of nonintersecting curves, or fibers, such that every point maps to a unique curve. Similar to the case of the straight bundles in R^3 above, the fibrations of interest here are also equipped with an important property that every fiber is associated with a unique point on a lower dimensional manifold (a 2D surface), such that distance between fibers in S^3 (i.e., the distance of closest approach) is encoded in metric properties of the surface, known as a *base*.

The topological and metric properties of the 3-sphere are encoded in the following toroidal coordinates:

$$\begin{aligned} x_1 &= \Omega^{-1}\cos\phi\sin\Theta, \\ x_2 &= \Omega^{-1}\sin\phi\sin\Theta, \\ x_3 &= \Omega^{-1}\cos\psi\cos\Theta, \\ x_4 &= \Omega^{-1}\sin\psi\cos\Theta, \end{aligned}$$

a parametrization that satisfies Eq. (28) by construction. Surfaces of fixed Θ are periodic under $\phi \to \phi + 2\pi$ and $\psi \to \psi + 2\pi$ and therefore have the topology of 2D tori. In these coordinates the metric of S^3 has a simple form,

$$dx_i^2 = \Omega^{-2}(\sin^2\Theta d\phi^2 + \cos^2\Theta d\psi^2 + d\Theta^2) \text{ in } S^3, \tag{29}$$

which shows that the metric of fixed Θ surfaces is Euclidean and spans a rectilinear periodic cell of dimensions $2\pi\Omega^{-1}\sin\Theta$ and $2\pi\Omega^{-1}\cos\Theta$, along the ϕ and ψ directions, respectively [see Fig. 13(a)]. Fibers, or filament backbones, are curves running along surfaces of constant Θ parametrized by

$$\phi(\psi) = \phi_0 + \alpha\psi. \tag{30}$$

Here ψ plays the role of an arc coordinate, describing different positions along the filament backbone, and α is the number turns of the fiber around the ϕ direction per rotation around the ψ direction [see Fig. 13(a)]. It is straightforward to show that any two such curves sharing the same α (at different ϕ_0) remain equidistant along their entire length.

As with the case of the straight bundles in R^3 the interfilament metric may be deduced by considering the length $\ell(\Theta)$ of a curve separating points of self-contact along a given fiber in S^3 which defines the "perimeter" or the amount of space available for packing fibers along the ϕ direction at fixed Θ.[5]

[5]This notion of perimeter neglects self-contact with any periodic images of the fiber that may pass between ϕ_0 and $\phi_0 + 2\pi$. For example, for $\alpha = n/m$ (where n and m are relatively prime integers) a fiber will wind n times around the ϕ direction for every m turns around the ψ, leading to n copies of the fiber section between ϕ_0 and $\phi_0 + 2\pi$, which clearly limit the number of filaments of a given diameter that can be packed on the 2-torus. Because the implicit n-fold symmetry of the fibration around ϕ has been neglected at this stage, some care must be taken when applying this result to packings, specifically, every filament in the packing must be associated with the $n-1$ copies spaced at intervals of $2\pi/n$. In their analysis of metric properties of S^3, Charvolin and Sadoc retain the n-fold images of a fiber when constructing the $\ell(\Theta)$ leading to a somewhat modified formula for the base metric.

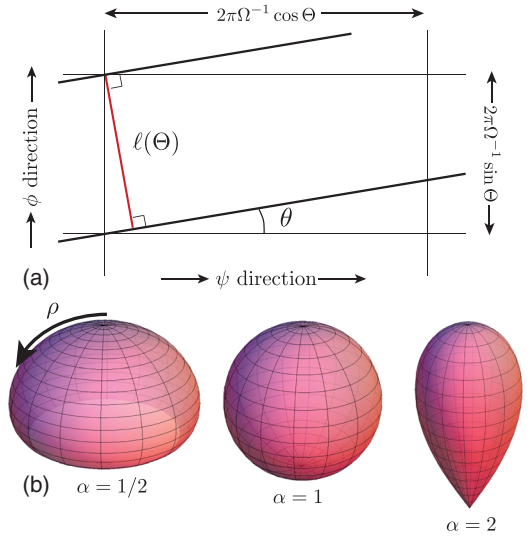

FIG. 13 (color online). (a) The toroidal coordinate system of fibrations in S^3, showing the dimensions of the T^2 unit cell at fixed Θ. Fibers (filament backbones) wind along the dark solid lines at an angle θ with respect to the $\hat{\psi}$ axis. The perimeter is defined as the distance of closest contact between the fiber at ϕ and its periodic image at $\phi + 2\pi$. (b) Surfaces (bases) carrying the interfilament metric of fibrations in S^3.

As shown in Fig. 13, this is easily reduced to $\ell(\Theta) = 2\pi\Omega^{-1}\cos\theta\sin\Theta$, where $\theta = \arctan(\alpha\tan\Theta)$ is the "tilt angle" of the fiber on the 2-torus at Θ. Hence,

$$\ell(\Theta) = 2\pi\Omega^{-1}\frac{\sin\Theta\cos\Theta}{\sqrt{\cos^2\Theta + \alpha^2\sin^2\Theta}}. \tag{31}$$

Using this perimeter and noting the distance between fibers at different Θ is simply $\Omega^{-1}|d\Theta|$, we have the interfiber metric

$$d\Delta^2_*(\alpha) = (2\Omega)^{-2}\left[d(2\Theta)^2 + \frac{\sin^2(2\Theta)d\phi_0^2}{\cos^2\Theta + \alpha^2\sin^2\Theta}\right] \text{ in } S^3. \tag{32}$$

This metric formula shows that the geometry of the base surface for twisted fibrations of S^3, like that of the case of straight, twisted bundles in R^3, is axisymmetric, with $\Omega^{-1}\Theta$ the arc distance from a pole at $\Theta = 0$. Again, the independence of the interfilament metric on ψ derives from the equidistance of any pair of curves sharing the same α.

The particular case of $\alpha = 1$ corresponds to the celebrated *Hopf fibration* (Sadoc and Mosseri, 2008), where each fiber is a closed geodesic of S^3 (great circle) which winds (twists) around its neighbor once every cycle from ψ to $\psi + 2\pi$. The interfiber metric has the remarkably simple form $d\Delta^2_*(\alpha = 1) = (2\Omega)^{-2}[d(2\Theta)^2 + \sin^2(2\Theta)d\phi_0^2]$, identical to the geodesic distance measured between points on a 2-sphere of radius $(2\Omega)^{-1}$, with polar and azimuthal angles 2Θ and ϕ_0, respectively. In this unique geometry ($\alpha = 1$), packing double-twisted filaments in S^3 maps identically onto the generalized Thomson problem of packing points on S^2 (Altschuler *et al.*, 1997; Saff and Kuijaars, 1997). Exploiting the homogeneous metric geometry of the Hopf fibration, Kléman constructed a class of ideal twisted filament packings in S^3, such that all nearest-neighbor filaments are closely packed, at a center-to-center spacing equal to the diameter d (Kléman, 1985). Evenly spaced distributions of disks on S^2 are possible only for certain numbers of disks, or, equivalently, for certain ratios of diameter to sphere radius $2\Omega d$, packings which correspond to the vertices of the Platonic solids which possess only a small number of disks ($\lesssim$20). By mapping the Hopf packings in S^3 to their associated "Platonic" packing on S^2 (shown in Fig. 14) Kléman showed that the densest such packing of twisted filaments has icosahedral symmetry with each filament surrounded by five neighbors (Kléman, 1985).

The cases of $\alpha \neq 1$ provide generalizations of the Hopf fibration, known as *Siefert fibrations* (Sadoc and Charvolin, 2009). When $\alpha \neq 1$, the fibers are not geodesics of S^3, although they remain closed curves for any rational α. Examples of the 2D base (embedded in R^3) are shown in Fig. 13(b), where we take $\rho = \Omega^{-1}\Theta$ to be the arc distance from the pole at $\Theta = 0$, and define the Euclidean distance from the z axis of radial symmetry to be

$$r_\perp(\rho) = \frac{\sin(2\Omega\rho)}{2\Omega\sqrt{1 + (\alpha^2 - 1)\sin^2(\Omega\rho)}}. \tag{33}$$

From this metric, it is straightforward to show that the Gaussian curvature at the pole has the following form:

$$K_G(\rho = 0) = \Omega^2(1 + 3\alpha^2) \text{ in } S^3, \tag{34}$$

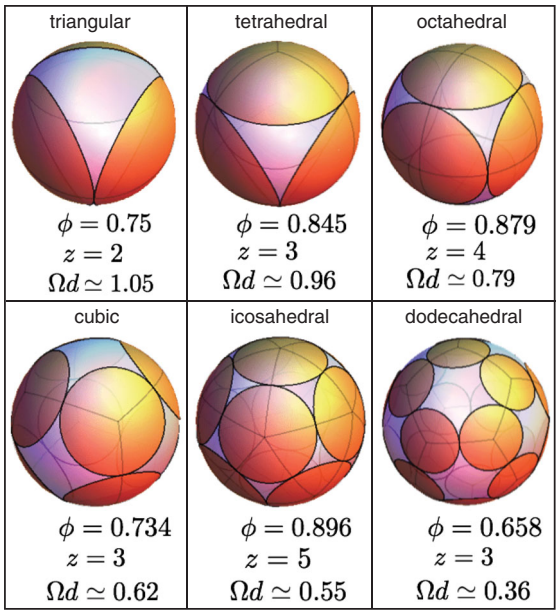

FIG. 14 (color online). The ideal packings of twisted and equally spaced filaments (diameter d) in S^3 whose positions correspond to vertices of Platonic solids projected on S^2, where ϕ, Ωd, and z denote packing fraction, reduced twist, and coordination number of the packing. From Kléman, 1985.

which is consistent with the apparent increase of curvature with α seen in Fig. 13(b).[6] Note that for $\alpha \neq 1$, the 2D surface is not smoothly embeddable in R^3. For $\alpha < 1$, the surface cannot be extended beyond a cusp at ρ_m where $|\partial_\rho r_\perp(\rho_m)| = 1$, while for $\alpha > 1$ a conical singularity develops at the $\Theta = \pi/2$ (or $\rho = \Omega^{-1}\pi/2$) pole. To date, optimal packing geometries on these base metrics of Seifert fibrations for $\alpha \neq 1$ have not been studied.

B. Projecting ideal packings to Euclidean space

In principle, the high symmetry of the interfiber distances of the fibrations of S^3 (all fibers are equidistant and metrics are axisymmetric) provides a natural setting for investigating optimal packings of twisted filaments with a more complex topology than the straight, twisted bundle described in Sec. III. However, exploiting the ideal properties of fibrations of S^3 in models of filament packing in Euclidean space requires overcoming at least two critical challenges. First, for a given filament number, α, Ω, and a model of filament interactions, the optimal filament packing must be identified, which is the analog of the generalized Thomson problem defined for the broader class of base surfaces. Provided these optimized packings can be determined for S^3, an additional step is needed to "rescue" the filament configurations from curved space (S^3), via some projection to R^3, which in turn alters the interfilament distances form their ideal geometry in R^3. As it is not possible to project from curved to a flat space while globally preserving distance properties, one might view the choice of projection from S^3 to R^3 as a second, and currently unsolved, step of the optimization procedure.

One approach that was suggested by Charvolin and Sadoc (2008) is based on the stereographic projection from S^3 to R^3. Because it is conformal, the stereographic projection has the advantage of preserving angular properties, including the skew angle of neighboring filaments in the double-twisted packing. Furthermore, the metric distortion from the optimal geometry of S^3 vanishes near the projected pole of the stereographic image, such that appropriate choices of the projection pole allow different (finite) regions of the S^3 packing to be projected to R^3 with a nominal distortion of interfilament spacing. For example, a projection that generates toroidal bundles and preserves the curved-space metric along their center lines takes x_1 as the projection axis so that filament positions in Euclidean coordinates become

$$x(s) = \frac{x_3(s)}{1-\Omega x_1(s)}, \qquad y(s) = \frac{x_4(s)}{1-\Omega x_1(s)}, \qquad z(s) = \frac{x_2(s)}{1-\Omega x_1(s)}. \tag{35}$$

Under this projection, the filaments wind around a family of nested tori. The central axis of the torus is the $\hat{z}$ axis and toroidal coordinates—a is the "major radius," or the distance of torus center from the axis and ρ is the "minor radius," or the radial distance of the torus surface from the torus center (as in Fig. 15)—related to S^3 coordinates by

$$\rho(\Theta) = \Omega^{-1}\tan\Theta, \qquad a(\Theta) = \Omega^{-1}\sec\Theta. \tag{36}$$

Hence, the pole at $\Theta = 0$ maps to the planar circle of radius Ω^{-1}, and the pole at $\Theta = \pi/2$ maps to the central (z) axis (infinite radius circle). As the stereographic projection is conformal, the angle θ between the axial direction and filament tangents winding around fixed-Θ tori remains constant, $\tan\theta = \alpha\tan\Theta$. The interfilament metric of the stereographic projection has the form

$$d\Delta_*^2(\alpha) = \frac{\omega^2}{(2\Omega)^2}\left[d(2\Theta)^2 + \frac{\sin^2(2\Theta)d\phi_0^2}{\cos^2\Theta + \alpha^2\sin^2\Theta}\right] \text{ in } R^3, \tag{37}$$

which is identical to the metric in S^3, Eq. (32), up to the conformal factor describing a locally isotropic scaling of dimensions:

$$\omega = \frac{1}{1-\cos(\phi_0+\alpha\psi)\sin\Theta}. \tag{38}$$

For filament packings, this conformal factor represents the failure of the projected fibrations to maintain equidistance (as ψ advances) along their length. Filament positions on the inner (outer) side of the torus correspond to $\cos(\phi_0+\alpha\psi) > 0$ (<0), and hence $\omega > 1$ (<1) describes the measure of over-(under)crowding in toroidal packing, an effect which increases in magnitude for tori of large minor radius, or larger Θ [see, for example, projections in Fig. 16(a)]. Geometrically, the variation of interfilament spacing can be understood in terms of the difference between inner and outer spacing between consecutive, nonconcentric toroidal layers, as well as non-uniform angular rotation of filament positions around the

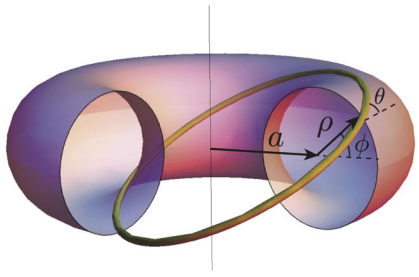

FIG. 15 (color online). Toroidal coordinates under stereographic projection to R^3. Surfaces of constant Φ are concentric tori, and fibers and filaments wind along these surfaces around both the minor and major axes of the tori, where θ is the (constant) angle between tangents and the circular axis of the torus. The circular fiber shown here corresponds to $\alpha = 1$, a projection of the Hopf fibration.

[6]Equation (34) also provides a direct illustration of O'Neill's theorem (Berger, 2003), which equates the Gaussian curvature of the base surface of a fibration to the sum ambient curvature of the embedding space (here Ω^{-2}) and 3 times the squared twist of the fibration [here $(\alpha\Omega)^2$]. Notice that the same formula holds for the straight twisted bundle in Euclidean space (zero ambient curvature).

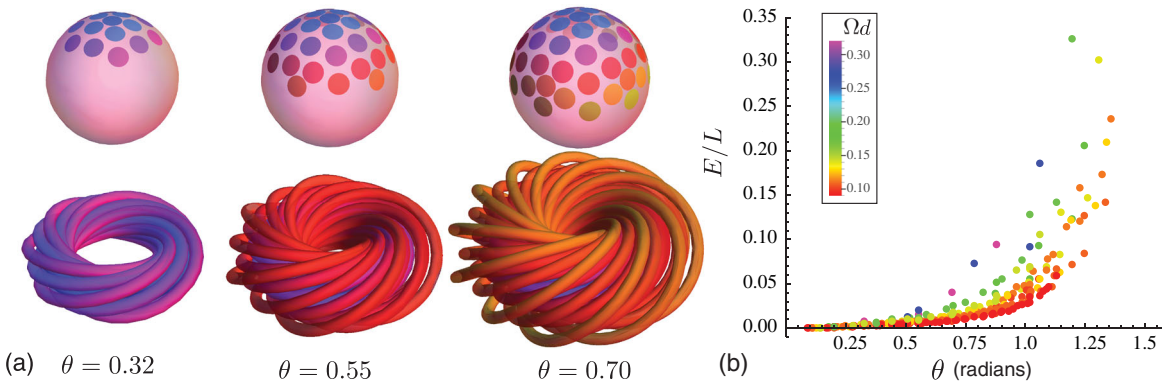

FIG. 16 (color online). (a) Stereographic projections of twisted filament packings in S^3 to R^3, based on the Hopf vibration ($\alpha = 1$). Filament positions on the S^2 base derive from the icosodeltahedral tesselations, where the value of Ωd is chosen based on the distance between the central filament (at the pole in S^2) and its first shell of neighbors. (a) $\{2, 2\}$ packings are shown, both on S^2 (top) and projections to R^3 (bottom). Left to right shows examples with increasingly larger maximum Φ, corresponding to larger polar distance on S^2, larger toroidal thickness, and larger twist angles of the outermost filaments. (b) The strain energy density defined by Eq. (39) and calculated numerically and plotted vs the twist angle of the outer filaments for icosodeltahedral tesselations, for a range of tesselations from small twist $\Omega_{\{4,2\}} = 0.0895d^{-1}$ to large twist $\Omega_{\{1,1\}} = 0.325d^{-1}$.

central axis of the tori required to maintain constant θ around a torus.

As a consequence of the conformal distortion of interfilament spacing, the optimality of ideal packings in S^3 when projected stereographically to R^3 becomes compromised, increasingly so as Θ increases. In particular, it is unclear at which point distortions of interfilament spacing become sufficiently large that the ideal packings identified in S^3 fail to provide an accurate model, even at a qualitative level, of the constraints and energetic consequence of packing in twisted toroidal bundles.

Absent a projection from curved space that preserves the equidistance of fibers in R^3, one can nevertheless consider the energetic costs of interfilament strains as a measure of the excess frustration cost of *bending* a twisted bundle into a torus. Setting aside the extent to which this excess cost could be relaxed by local or global adjustments of filament position and orientation in packing, we illustrate this cost for the class of toroidal bundles projected from the Hopf fibration ($\alpha = 1$).

The stereographic projection of the Hopf fibration has the feature that filament trajectories, which are (great) circles in S^3, are mapped to circles in R^3 (see, e.g., the filament in Fig. 15). This fact and the formula for the closest distance from the point to a circle of known center, orientation, and radius[7] greatly simplify calculations of interfilament distances in a projected Hopf packing. In R^3, these circular filaments have radius $p(\Phi) = \Omega^{-1} \sec\Theta$, they lie in planes tilted (transverse to the radial direction extending from $x = y = 0$ axis) by Θ relative to $\hat{z}$, and their centers sit at $\mathbf{x}_c(\Phi) = \rho(\Phi)(\sin\phi_0\hat{x} - \cos\phi_0\hat{y})$ such that they conform to the fixed-Θ tori. Using this geometry to compute the distance $\Delta_{ij}(s_i)$ between the ith filament at s_i along its length and the jth filament in terms of given coordinates (Θ_i, ϕ_i) and (Θ_j, ϕ_j) we consider a simple "elastic" model for the cost to interfilament cohesion due to interfilament strain,

$$E = \frac{1}{2}\sum_i \sum_{j\in\langle ij\rangle} \int ds_i |\Delta_{ij}(s_i) - d|^2, \tag{39}$$

where the second sum runs over the nearest neighbors in a given packing to i and d is the filament diameter. As a proxy for the optimal packings of N cohesive disks on S^2, we take the positions of *icosadeltahedral tesselations* of sphere (Šiber, 2007). These tesselations, familiar to structural models of spherical viruses (Caspar and Klug, 1962) and fullerenes (Kroto, 1997), are constructed from triangular tilings of icosohedra projected normally onto S^2 and are parametrized by the integer pair $\{m, n\}$ that describe the vector on separating centers of fivefold coordination (Šiber, 2007).

Figure 16(b) shows the packing energy per unit length E/L of stereographically projected Hopf bundles possessing icosadeltahedral order, where $L = \sum_i \int ds_i$ is the total Euclidean length of filaments in the bundle. The strain energy density is plotted versus twist angle $\theta = \Theta$ of outer filaments for icosodeltahedral tesselations, for a range of tesselations from small twist $\Omega_{\{4,2\}} = 0.0895d^{-1}$ to large twist $\Omega_{\{1,1\}} = 0.325d^{-1}$. Notably, the strain energy falls to zero as $\theta \to 0$, when the width of the bundles is small compared with the radius torus backbone, owing to the small conformal distortion near the $\Phi = 0$ pole of the projection. The characteristic increase in strain energy with twist in this case is not a symptom of the imperfect packing topology of filaments, as all $\theta \to \pi/2$ packings possess the topologically appropriate 12 five-coordinated sites needed for tessellations of S^2. Rather, the increase in strain with θ in these projected Hopf packings is a reflection of the fact that filament spacings in the projection become locally over- (under)dense on the inside (outside) of

[7]The nearest distance Δ_* of a point $\mathbf{x}_0$ to a circle of radius p in a plane normal to $\mathbf{N}$ centered at $\mathbf{x}_c$ is given by $\Delta_*^2 = \Delta_\parallel^2 + (p - \Delta_\perp)^2$, where $\Delta_\parallel = (\mathbf{x}_0 - \mathbf{x}_c)\cdot\mathbf{N}$ and $\Delta_\perp^2 = |\mathbf{x}_0 - \mathbf{x}_c|^2 - \Delta_\parallel^2$.

toroidal packing, and that conformal strain grows with toroidal thickness, roughly as $1-\omega \sim \sin\theta$ for small θ. It remains an open question how well ideal packings in S^3 provide quantitatively accurate pictures of twisted toroidal ground states in Euclidean space. That is, at large θ, is it sufficient to relax elastic strain via smooth deformations of filament positions in projected packings, or, instead, is the topological framework of the projected packings of S^3 wholly inadequate for modeling optimal structure in large-θ bundles in R^3?

V. CONCLUDING REMARKS

In conclusion, we presented an emerging theoretical perspective on the unique metric geometry of complex, multifilament or multicolumn assemblies. These studies show a powerful connection between the geometry of interfilament spacing and the metric geometry of non-Euclidean surfaces. The relationship between packing problems in filamentous assemblies with "incompatible" textures and packing problems on intrinsically curved surfaces is particularly valuable because physical models of optimal structure in the latter class of problems are well established, and the coupling between Gaussian curvature and topological defects in 2D membranes has received wide study in recent decades (Bowick and Giomi, 2009). Drawing on these familiar analogs sheds new light on the surprising rich, and largely overlooked, questions of optimal structure in filamentous and columnar matter. Furthermore, the purely geometrical origin of the frustration between patterns of orientation and spacing leads to a rich set of nontrivial and universal predictions for long-range order in a broad class of materials. In particular, the optimal topological charge of the twisted packing was shown to be a universal function of a single geometric parameter, θ the tilt angle at the bundle surface, remarkably independent of elementary microscopic properties like filament interactions or diameter. Considerations of interfilament metric geometry are broadly applicable across material systems and material scales, and we anticipate, therefore, that the robust and geometrical origin of these predictions will aid in their direct experimental test.

Numerous examples of twisted molecular filament assemblies exist in biological and synthetic materials. Yet, to date, the specific structure of interfilament packing, particularly topological defects in the interfilament order, in these materials has received little experimental study. This is due, in part, to extreme contrast of length scales presented by these materials in combination with the intrinsic variation of ordering introduced by twisted structures. For example, collagen fibrils are formed from triple-helical polypeptide chains, procollagen molecules roughly 1 nm in diameter, assembled into mesoscopically large structures, ranging in the 100s of nanometers (Wess, 2008). Understanding small-angle scattering studies of the form factor of collagen fibrils has been confounded by the fact that locally "crystalline" domains of procollagen are apparently nonuniformly oriented throughout fiber, and, further, the "best-fit" models to date imply the coexistence of some measure of crystalline and noncrystalline packing (Hulmes *et al.*, 1995; Charvolin and Sadoc, 2011). High-resolution electron microscopy has improved the "real space" collagen packing model somewhat (Orgel *et al.*, 2006), resolving lateral motifs on the few-filament scale ($\sim 3-5$), yet the global organization of these local motifs within heterogeneous (and twisted) fibrils as wide as 100s of individual filaments across remains inadequately understood.

Notwithstanding these challenges, the expanding resolution range offered by state of the art microscopy techniques down to nanometer and subnanometer scale provides an exciting opportunity to test universal predictions for geometrically frustrated fibers and poses important, new challenges for their theoretical understanding. For example, recent high-resolution cryotransmission electron miscroscope (cryoTEM) studies of DNA confined within bacteriophage capsids by Leforestier and Livolant (2009) revealed a surprisingly detailed picture of interstrand organization taking place within what is clearly a highly frustrated and heterogeneous packing. DNA chains exhibit the seemingly contradictory combination of locally sixfold (hexagonal) packing, a high degree of order, and high density throughout the roughly spherical volume. While current imaging achieves substrand resolution only within transverse 2D sections, full three-dimensional reconstruction of the positions and orientations through such a complex packing may soon be achievable.

Understanding the interplay between the texture induced by spherical confinement and the complex spectrum of topological defects in the transverse packing in a maximally dense assemblies, what might be viewed as the filamentous analog to the Thomson problem, introduces several key challenges. Specifically, how are constraints of interfilament metric geometry formulated under conditions where the texture itself varies throughout? No doubt, a fully rotationally invariant formulation of the elasticity of columnar structures is needed in order tackle optimal structure where assumptions about small tilt relative to a well-defined (and effectively Euclidean) reference state cannot be maintained. While no fundamental obstacles stand in the way of formulating a rotationally invariant theory for columnar elasticity, it remains to be seen how well such a theory may illuminate properties of optimal packing where interfilament metric geometry cannot be reduced to a single curved 2D manifold. Instead new frameworks may be required for optimizing packing over a sequence of inequivalent surfaces representing variation of interfilament texture throughout structures as complex as confined, contorted, and folded chain packings exhibited by DNA.

ACKNOWLEDGMENTS

I am grateful to collaborators A. Azadi and I. Bruss for numerous discussions and insights on topics reviewed in this Colloquium. Further, I thank L. Cajamarca, R. Kamien, J.-F. Sadoc, D. Sussman, and P. Ziherl for critical readings of this manuscript, and O. Lavrentovich for discussions valuable for stimulating this Colloquium. This work was supported by the NSF CAREER Award No. DMR 09-55760 and through an award from the Alfred P. Sloan Foundation.

REFERENCES

Alberts, B., A. Johnson, J. Lewis, M. Raff, K. Roberts, and P. Walter, 2002, *Molecular Biology of the Cell* (Garland Science, New York), 4th ed.

Altschuler, E. L., T. J. Williams, E. R. Ratner, R. Tipton, R. Stong, F. Dowla, and F. Wooten, 1997, Phys. Rev. Lett. **78**, 2681.

Azadi, A., and G. M. Grason, 2012, Phys. Rev. E **85**, 031604.

Azadi, A., and G. M. Grason, 2014, Phys. Rev. Lett. **112**, 225502.

Bausch, A. R., M. J. Bowick, A. Cacciuto, A. D. Dinsmore, M. F. Hsu, D. R. Nelson, M. G. Nikolaides, A. Travesset, and D. A. Weitz, 2003, Science **299**, 1716.

Berger, M., 2003, *A Panoramic View of Riemannian Geometry* (Springer-Verlag, Berlin).

Bernal, J. D., and J. Mason, 1960, Nature (London) **188**, 910.

Bouligand, Y., 2008, C.R. Chim. **11**, 281.

Bouligand, Y., J.-P. Denefle, J.-P. Lechaire, and M. Maillard, 1985, Biol. Cell **54**, 143.

Bowick, M. J., and L. Giomi, 2009, Adv. Phys. **58**, 449.

Bowick, M. J., D. R. Nelson, and A. Travesset, 2000, Phys. Rev. B **62**, 8738.

Bruss, I. R., and G. M. Grason, 2012, Proc. Natl. Acad. Sci. U.S.A. **109**, 10781.

Bruss, I. R., and G. M. Grason, 2013, Soft Matter **9**, 8327.

Bugayevsky, L. M., and J. P. Snyder, 1995, *Map Projections: A Reference Manual* (Taylor and Francis, Philadelphia).

Caspar, D. L. D., and A. Klug, 1962, Cold Spring Harbor Symp. Quant. Biol. **27**, 1.

Chaikin, P. M., and T. C. Lubensky, 1995, *Principles of Condensed Matter Physics* (Cambridge University Press, Cambridge, England).

Charvolin, J., and J.-F. Sadoc, 2008, Eur. Phys. J. E **25**, 335.

Charvolin, J., and J.-F. Sadoc, 2011, Biophys. Rev. Lett. **06**, 13.

Che, S., Z. Liu, T. Ohsuna, K. Sakamoto, O. Terasaki, and T. Tatsumi, 2004, Nature (London) **429**, 281.

Cooper, A., 1969, Biochem. J. **112**, 515 [http://www.biochemj.org/bj/112/bj1120515.htm].

Costello, G. A., 1997, Theory of Wire Rope (Springer-Verlag, New York), 2nd ed.

de Gennes, P. G., and J. Prost, 1993, *The Physics of Liquid Crystals* (Claredon Press, Oxford), 2nd ed.

de Gennes, P.-G., 1972, Solid State Commun. **10**, 753.

do Carmo, M. P., 1976, *Differential Geoemetry of Curves and Surfaces* (Prentice-Hall, Englewood Cliffs), Chap. 4.

Douglas, J. F., 2009, Langmuir **25**, 8386.

Foster, J. A., M.-O. Piepenbrock, G. O. Lloyd, N. Clarke, J. A. K. Howard, and J. W. Steed, 2010, Nat. Chem. **2**, 1037.

Galileo, G., 1914, *Dialogues Concerning Two New Sciences* (MacMillan, New York).

Goodby, J. W., 1991, J. Mater. Chem. **1**, 307.

Goodby, J. W., 2012, Proc. R. Soc. A **468**, 1521.

Grason, G. M., 2009, Phys. Rev. E **79**, 041919.

Grason, G. M., 2010, Phys. Rev. Lett. **105**, 045502.

Grason, G. M., 2012, Phys. Rev. E **85**, 031603.

Grason, G. M., and R. F. Bruinsma, 2007, Phys. Rev. Lett. **99**, 098101.

Grason, G. M., and B. Davidovitch, 2013, Proc. Natl. Acad. Sci. U.S.A. **110**, 12893.

Hales, T. C., 2000, Not. Am. Math. Soc. **47**, 440 [http://www.ams.org/notices/200004/fea-hales.pdf].

Hamley, I. W., 2010, Soft Matter **6**, 1863.

Harris, A. B., R. D. Kamien, and T. C. Lubensky, 1999, Rev. Mod. Phys. **71**, 1745.

Hearle, J. W. S., P. Grosberg, and S. Backer, 1969, *Structural Mechanics of Fibers, Yarns, and Fabricss*, Vol. 1 (Wiley-Interscience, New York).

Heussinger, C., and G. M. Grason, 2011, J. Chem. Phys. **135**, 035104.

Hud, N. V., and K. H. Downing, 2001, Proc. Natl. Acad. Sci. U.S.A. **98**, 14925.

Hud, N. V., K. H. Downing, and R. Balhorn, 1995, Proc. Natl. Acad. Sci. U.S.A. **92**, 3581.

Hulmes, D. J., T. J. Wess, D. J. Prockop, and P. Fratzl, 1995, Biophys. J. **68**, 1661.

Irvine, W. T., V. Vitelli, and P. M. Chaikin, 2010, Nature (London) **468**, 947.

Jeong, J., Z. S. Davidson, P. J. Collings, T. C. Lubensky, and A. J. Yodh, 2014, Proc. Natl. Acad. Sci. U.S.A. **111**, 1742.

Kamien, R. D., 2002, Rev. Mod. Phys. **74**, 953.

Kamien, R. D., and D. R. Nelson, 1995, Phys. Rev. Lett. **74**, 2499.

Kamien, R. D., and D. R. Nelson, 1996, Phys. Rev. E **53**, 650.

Kléman, M., 1980, J. Phys. France **41**, 737.

Kléman, M., 1985, J. Phys. Lett. **46**, 723.

Kléman, M., 1989, Adv. Phys. **38**, 605.

Knobler, C. M., and W. Gelbart, 2009, Annu. Rev. Phys. Chem. **60**, 367.

Kouwer, P. H. J., *et al.*, 2013, Nature (London) **493**, 651.

Kroto, H., 1997, Rev. Mod. Phys. **69**, 703.

Lee, C. C., C. Grenier, E. W. Meijer, and A. P. H. J. Schenning, 2009, Chem. Soc. Rev. **38**, 671.

Leforestier, A., and F. Livolant, 2009, Proc. Natl. Acad. Sci. U.S.A. **106**, 9157.

Leforestier, A., and F. Livolant, 2010, J. Mol. Biol. **396**, 384.

Livolant, F., and A. Leforestier, 1996, Prog. Polym. Sci. **21**, 1115.

Livolant, F., A. M. Levelut, J. Doucet, and J. P. Benoit, 1989, Nature (London) **339**, 724.

Makowski, L., and B. Magdoff-Fairchild, 1986, Science **234**, 1228.

McQuarrie, D. A., 2000, *Statistical Mechanics* (University Science Books, Sausalito), Chap. 14.

Millman, R. S., and G. D. Parker, 1977, *Elements of Differential Geometry* (Prentice-Hall, Englewood Cliffs, NJ).

Nelson, D. R., 2002, *Defects and Geometry in Condensed Matter Physics* (Cambridge University Press, Cambridge, England).

Nelson, D. R., and L. Peliti, 1987, J. Phys. (Orsay, Fr.) **48**, 1085.

Neukrich, S., and G. H. M. van der Heijden, 2002, J. Elast. **69**, 41.

Neville, A. C., 1993, *Biology of Fibrous Composites: Development Beyond the Cell Membrane* (Cambridge University Press, Cambridge, England).

O'Hern, C. S., L. E. Silbert, A. J. Liu, and S. R. Nagel, 2003, Phys. Rev. E **68**, 011306.

Olsen, K., and J. Bohr, 2010, Theor. Chem. Acc. **125**, 207.

Olsen, K., and J. Bohr, 2011, Europhys. Lett. **93**, 60004.

Orgel, J. P. R., T. C. Irving, A. Miller, and T. J. Wess, 2006, Proc. Natl. Acad. Sci. U.S.A. **103**, 9001.

Ottani, V., D. Martini, M. Franchi, A. Ruggeri, and M. Raspanti, 2002, Micron **33**, 587.

Pan, N., 2014, Appl. Phys. Rev. **1**, 021302.

Pan, N., and D. Brookstein, 2002, J. Appl. Polym. Sci. **83**, 610.

Peach, M., and J. S. Koehler, 1950, Phys. Rev. **80**, 436.

Renn, S. R., and T. C. Lubensky, 1988, Phys. Rev. A **38**, 2132.

Rubinstein, M., and D. R. Nelson, 1983, Phys. Rev. B **28**, 6377.

Sadoc, J.-F., and J. Charvolin, 2009, J. Phys. A **42**, 465209.

Sadoc, J.-F., and R. Mosseri, 2008, *Geometrical Frustration* (Cambridge University Press, Cambridge, England).

Saff, E. B., and A. B. J. Kuijaars, 1997, Math Intellegencer **19**, 5.

Selinger, J. V., and R. F. Bruinsma, 1991, Phys. Rev. A **43**, 2910.

Sethna, J. P., D. C. Wright, and N. D. Mermin, 1983, Phys. Rev. Lett. **51**, 467.

Seung, H. S., and D. R. Nelson, 1988, Phys. Rev. A **38**, 1005.

Shin, H., and G. M. Grason, 2011, Europhys. Lett. **96**, 36007.

Šiber, A., 2007, arXiv:0711.3527.

Starostin, E. L., 2006, J. Phys. Condens. Matter **18**, S187.

Svenšek, D., G. Veble, and R. Podgornik, 2010, Phys. Rev. E **82**, 011708.
Tortora, L., and O. D. Lavrentovich, 2011, Proc. Natl. Acad. Sci. U.S.A. **108**, 5163.
Weisel, J. W., 2004, Biophys. Chem. **112**, 267.
Weisel, J. W., C. Nagawami, and L. Makowski, 1987, Proc. Natl. Acad. Sci. U.S.A. **84**, 8991.
Wess, T. J., 2008, *Biology of Fibrous Composites: Development Beyond the Cell Membrane* (Springer, Boston), Chap. 3.
Wright, D. C., and N. D. Mermin, 1989, Rev. Mod. Phys. **61**, 385.
Yang, S., L. Zhao, C. Yu, X. Zhou, J. Tang, P. Yuan, D. Chen, and D. Zhao, 2006, J. Am. Chem. Soc. **128**, 10460.
Yang, Y., R. B. Meyer, and M. F. Hagan, 2010, Phys. Rev. Lett. **104**, 258102.